Wind-driven interannual variability of sea ice algal production in the western Arctic Chukchi Borderland

Eiji Watanabe*[1], Jonaotaro Onodera[1], Naomi Harada[1], Maki Noguchi Aita[1], Akio Ishida[2], and Michio J. Kishi[3]

[1]*Japan Agency for Marine-Earth Science and Technology, Yokosuka, Japan*

2-15 Natsushima, Yokosuka, Kanagawa, 237-0061, JAPAN

Tel: +81-46-867-9480

E-mail: ejnabe@jamstec.go.jp

[2]*Department of Social and Environmental Studies, Tokoha University, Fuji, Japan*

[3]*Faculty of Fisheries Sciences, Hokkaido University, Hakodate, Japan*

Abstract

Seasonal and interannual variability in the biogenic particle sinking flux was recorded using multi-year bottom-tethered sediment trap mooring systems in the Northwind Abyssal Plain (Station NAP: 75°N, 162°W, 1975-m water depth) of the western Arctic Chukchi Borderland. Trapped particle flux at a median depth of 184 m had an obvious peak and dominance of sea ice-related diatom assemblages in August 2011. The observed particle flux was considerably suppressed throughout summer 2012. In the present study, the response of ice algal production and biomass to wind-driven changes in the physical environment was addressed using a pan-Arctic sea ice-ocean modeling approach. A sea ice ecosystem with ice algae was newly incorporated into the lower-trophic marine ecosystem model, which was previously coupled with a high-resolution (i.e., 5-km horizontal grid size) sea ice-ocean general circulation model. Seasonal model experiments covering two-year mooring periods indicated that primary productivity of ice algae around the Chukchi Borderland depended on basin-scale wind patterns via various processes. Easterly winds in the southern part of a distinct Beaufort High supplied nutrient-rich water for euphotic zones of the NAP region via both surface Ekman transport of Chukchi shelf water and vertical turbulent mixing with underlying nutricline water in 2011. In contrast, northwesterly winds flowing in the northern part of an extended Siberian High transported oligotrophic water within the Beaufort Gyre circulation toward the NAP region in 2012. The modeled ice algal biomass during summer reflected the differences in nutrient distribution. The modeled sinking flux of particulate organic nitrogen (PON) was comparable with the time series obtained from sediment trap data in summer 2011. In contrast, lateral advection of ice algal patches of shelf origin during a great cyclone event may have

caused a modeled PON flux bias in 2012. Extending the year-long measurements is expected to help illustrate the more general features of ice-related biological processes in the Arctic Ocean.

Keywords: Arctic Ocean, Northwind Abyssal Plain, ice algae model, primary production, wind pattern

1. Introduction

The response of biogeochemical cycles to the decline in Arctic sea ice has become an important topic for a variety of communities. Improved light conditions during summer have enhanced phytoplankton photosynthesis activity in the Eurasian pelagic area of the Arctic Ocean (Wassmann, 2011). A widespread massive deposition of ice algal biomass was detected on the deep seafloor of the eastern Arctic basin (Boetius et al., 2013). On the other hand, the under-ice export of particulate organic carbon (POC) was limited by insufficient nutrient supply in the stratified central Arctic (Lalande et al., 2014). In the Beaufort Gyre region of the western Arctic, freshwater accumulation suppressed primary production during the 2000s (McLaughlin et al., 2010; Nishino et al., 2011). It is necessary to fill in the observational gaps to understand spatial and temporal variability in the biological processes of the Arctic Ocean.

Sediment trap measurements are useful to capture year-long biological activity signals. The locations of bottom-tethered traps have been confined to the north of the Laptev Sea (Fahl and Nöthig, 2007), Mackenzie shelf (Forest et al., 2007), and the deep Canada Basin (Honjo et al., 2010; Hwang et al., 2015). In our field campaign, year-round bottom-tethered moorings, including sediment trap instruments, have been deployed in the Northwind Abyssal Plain (NAP) of the Chukchi Borderland since October 2010 (Fig. 1). Early-winter maxima of sinking particle flux with fresh organic material have been captured annually at Station NAP (75°N, 162°W, 1,975 m water depth) (Watanabe et al., 2014; Onodera et al., 2015). The substantial quantities of lithogenic minerals in the trapped particles suggest shelf-origin water transport toward the NAP region. Seasonal experiments using an eddy-resolving (5 km grid size) pan-Arctic sea ice-ocean model indicated the effective role of Beaufort shelf-break eddies in the transport of Chukchi shelf water with high biological productivity and in the consequent early-

63 winter peaks of sinking biogenic flux at Station NAP (Watanabe et al., 2014). It should be noted
64 that biological production continued inside these eddies moving in the southern Canada Basin.
65 Another finding obtained at Station NAP was remarkable interannual variability in summer
66 particle flux (Onodera et al., 2015; Ikenoue et al. 2015; Matsuno et al., 2015). Trapped particle
67 flux peaked sharply in August 2011 but was suppressed considerably during summer 2012. The
68 diatom assemblage compositions suggest that year-to-year changes in the distribution of shelf-
69 origin water and relatively oligotrophic water originating from the interior of the Canada Basin
70 controls the particle flux around the Chukchi Borderland (Onodera et al., 2015). This situation
71 was supported by ocean current fields simulated in a medium-resolution (25 km grid size)
72 framework by the pan-Arctic physical oceanographic model (Onodera et al., 2015). However,
73 reliable *in-situ* biological productivity and water mass transport data above the shallow trap
74 depth (approximately 180–260 m) could not be available at Station NAP during the mooring
75 periods (October 2010–September 2012). In particular, chlorophyll, nutrient concentration, and
76 ocean velocity data from winter to early summer were insufficient. Further detailed
77 investigation of the background mechanisms associated with summer biogenic flux would be
78 highly valuable and possible using a coupled physical and marine ecosystem model. Whereas
79 the main content of observed diatom valves was the sea ice-related species (e.g., *Fossula*
80 *arctica*, Onodera et al., 2015), sea ice ecosystem was not included in our previous model
81 experiment (Watanabe et al., 2014). The lack of ice algae was a plausible factor for the summer
82 delay of the simulated biogenic flux peak behind the trap data. These issues raised our
83 motivation to incorporate ice-related biogeochemical processes in the model.
84 Ice algae models have a long history of development. Pioneering work was conducted on
85 the Antarctic fast ice ecosystem (Arrigo et al., 1993). For the Arctic Ocean, one-dimensional ice

86 algae models were applied to landfast ice in Resolute Passage of the Canadian Archipelago
87 (Lavoie et al., 2005; Pogson et al., 2011) and offshore Barrow (Jin et al., 2006). The modeled
88 region has been extended in recent years to include the entire Arctic Ocean (Dupont, 2012) and
89 global domain (Deal et al., 2011; Jin et al., 2012). The analysis period covered from seasonal
90 transition (Lavoie, 2005; Deal et al., 2011) to decadal variability (Jin et al., 2012; Dupont,
91 2012) and future projections (Lavoie et al., 2010). Most models assume that ice algal activity
92 occurs primarily in the skeletal layer of the sea ice bottom (i.e., ice-water interface), where the
93 layer thickness is fixed at 2 cm (Lavoie et al., 2005), 3 cm (Jin et al., 2012), and 5 cm (Dupont,
94 2012). The ice algal biomass sometimes reaches values three orders of magnitude larger at the
95 ice-water interface than that in the upper part of the sea ice column (e.g., Jin et al., 2006).
96 Ocean surface water is a major nutrient supplier for ice algae in the skeletal layer. Tidal mixing
97 controls nutrient exchange rates at the ice-water interface in the narrow shallow straits of the
98 Canadian Archipelago (Lavoie et al., 2005). In a general viewpoint, it is reasonable that nutrient
99 flux is calculated as a function of the sea ice freezing/melting rate (Arrigo et al., 1993; Jin et al.,
100 2006). However, Dupont (2012) did not calculate nutrient import due to sea ice freezing,
101 following an observational view where nutrients trapped inside the sea ice column have minor
102 contributions to an ice algal bloom (Cota et al., 1991; Cota and Smith, 1991). As grazing
103 pressure on ice algae is considered weak in the sea ice column, most previous models excluded
104 zooplankton biology in the skeletal layer (Jin et al., 2006; Dupont, 2012) or prescribed a small
105 grazing rate to potential grazers (e.g., amphipods) (Lavoie, 2005). The habitat of ice algae in the
106 skeletal layer disappears gradually due to melting sea ice. The assemblages released from the
107 sea ice bottom partially act as phytoplankton and become a food source for pelagic grazers in

the water column (Michel et al., 1993, 1996). Thus, complex ice algal processes have been proposed and numerically formulated in various ways.

In the present study, seasonal and interannual variability of ice algal production and biomass in the Chukchi Borderland were addressed using a pan-Arctic sea ice-ocean modeling approach (Fig. 1). We focused particularly on the relationships between ice-related biogeochemical processes and wind-driven dynamics, such as shelf-basin exchanges, local upwelling/downwelling, and vertical turbulent mixing. To represent the summer biogenic particle flux captured by sediment trap measurements, the simple sea ice ecosystem was newly incorporated into a lower-trophic marine ecosystem model. Our model coupled with a sophisticated high-resolution physical component is a powerful tool for the above-mentioned subjects because of following issues. The Chukchi Borderland is composed of complex topography such as long ridges, deep-sea plateaus, and steep shelf breaks. The sinking biogenic flux available for comparison was obtained from the single-point mooring measurements in this area. The source regions of surface water are distributed over the Chukchi Sea, the East Siberian Sea, and the Canada Basin. The water mass transports are closely related to shelf-basin boundary currents and baroclinic eddies. These complex topography and mesoscale hydrographic features have been unresolved by previous basin-scale ice algae models, which horizontal resolution was much coarser than the typical internal Rossby radius of deformation in the polar region. The linkages between wind patterns, light and nutrient preconditioning of ice algal bloom, and particle sinking are also unique viewpoints in the present work. Modeling configurations and sediment trap analyses are described in Section 2. Seasonal transitions of the modeled ice-ocean field, particularly those around the NAP region, are traced in Section 3. Relationships between the interannual variability in biogeochemical properties and wind

patterns are examined in Section 4. Uncertainties of the modeled processes are discussed in Section 5, based on sensitivity experiments. The obtained findings are summarized in Section 6.

2. Model configuration and experimental design

2.1 Physical oceanographic model

The physical part of the coupled sea ice-ocean model is the "Center for Climate System Research Ocean Component Model (COCO)" version 4.9 (Hasumi, 2006). The sea ice component includes a multi-thickness-category configuration based on that of Bitz et al. (2001) with a one-layer thermodynamic formulation (Bitz and Lipscomb, 1999), the linear-remapping method for category transfer (Lipscomb, 2001), and the elastic-viscous-plastic rheology (Hunke and Dukowicz, 1997). In addition to the open water category, the lower limit of sea ice thickness in each category is set to 10, 30, 60, 100, 250, and 500 cm, respectively (i.e., 7 categories). The ocean component is a free-surface general circulation model formulated using the advection scheme of Leonard et al. (1994) and the turbulence closure mixed-layer scheme of Noh and Kim (1999).

2.2 Marine ecosystem model

The COCO model was coupled with a lower-trophic marine ecosystem model, "North Pacific Ecosystem Model for Understanding Regional Oceanography (NEMURO)". The detailed configuration of the original NEMURO model, which represented pelagic plankton species (i.e., diatom, flagellate, and copepod), was described in Kishi et al. (2007). To address seasonality and interannual variability in ice algal production and biomass, a sea ice ecosystem was incorporated in the present work, (Fig. 2 and Table 1). In the developed model (called "Arctic NEMURO", hereafter), the habitat of ice algae is confined to the 2-cm skeletal layer. The biogeochemical variables in the sea ice component comprise ice algae (IA), ice-related fauna (IF), nitrate (NO3), ammonium (NH4), silicate (SIL), dissolved organic nitrogen (DON), particulate organic nitrogen (PON), and opal (OPL). Each model grid has a single value per

158 variable independent of the ice thickness category. As the sea ice bottom temperature is always
159 kept at the freezing point of underlying seawater, a relationship of Q_{10} = 2 adopted in the
160 present model did not have substantial impacts on biogeochemical cycles in the sea ice column.
161 The growth rate of ice algae (GR) is calculated depending on light condition (L) and nutrient
162 uptake (N_{up}) terms:

163 $$GR = GR_{max} \times L \times N_{up},$$

164 where the maximum growth rate GR_{max} is fixed at a constant value of 0.8 d^{-1}.

165 The light condition term followed the original NEMURO formulation:

166 $$L = I / I_{opti} \times \exp(1 - I / I_{opti}),$$

167 $$I = PAR_{frac} \times SW^{\downarrow} \times (1 - \alpha_{sfc}) \times \exp(- k_{snow} H_{snow} - k_{ice} H_{ice}),$$

168 where I is photosynthetically active radiation (PAR) in the skeletal layer. The conversion
169 coefficient from shortwave radiation to PAR (PAR_{frac}) is 0.43 following the previous models
170 (Zhang et al., 2010; Dupont, 2012) so that 43% of shortwave flux is available for
171 photosynthesis activity. Light transmission through the snow and sea ice columns is given by
172 downward shortwave radiation from atmosphere ($SW^{\downarrow}$), snow/ice surface albedo (α_{sfc}), column
173 thickness (H_{snow}, H_{ice}), and empirical extinction rates (k_{snow}, k_{ice}). The surface albedo (α_{sfc})
174 changes from 0.8 to 0.6 depending on snow/ice type and surface temperature during summer.
175 The light extinction rate (k_{snow}, k_{ice}) is set to 0.12 cm^{-1} for snow and 0.045 cm^{-1} for sea ice based
176 on Aota and Ishikawa (1982). According to this constant rate, for example, the light intensity in
177 the skeletal layer corresponds to approximately 10% (1%) of that absorbed into the surface of
178 sea ice with its thickness of 50 cm (100 cm) (Fig. 3a). The light transmission is calculated in
179 each thickness category (see the category arrangement in Section 2.1), and the under-ice
180 average intensity is then obtained in each model grid. A self-shading effect of ice algae is

neglected. For weak-light adaptation of ice algae, the optimal light intensity (I_{opti}) is set to 10 W m^{-2} (cf., 104 W m^{-2} for pelagic phytoplankton (Kishi et al., 2007)). A PAR of 5 and 20 W m^{-2} results in a light condition term of 0.82 and 0.73, respectively (Fig. 3b).

The vertical exchange of biogeochemical variables between the skeletal layer and the ocean surface layer (suffixed as SKL and OCN, respectively, hereafter) is formulated in a different manner for sea ice freezing and melting periods. During the freezing period, ocean-to-ice fluxes F_{OI} are proportional to sea ice freezing rate IFR:

$$F_{OI} = CF_{OI} \times (NO3, NH4, SIL, DON)_{OCN} \times IFR.$$

The proportional coefficient CF_{OI} is set to 0.3, since first-year ice salinity is able to reach approximately 30% of ocean salinity. In addition, all of the imported nutrients are accumulated only in the skeletal layer. The actual ice algae respond to nutrients concentrated in brine pockets and channels. However, the incorporation of such detailed structures in sea ice interiors is generally difficult for three-dimensional climate models. Here, we regard the skeletal layer as the reservoir of total imported nutrients under an idealized assumption. There is no import of particles such as pelagic planktons, PON, and OPL. During the melting period, ice-to-ocean fluxes F_{IO} are proportional to the sea ice melting rate IMR:

$$F_{IO} = (IA, IF, NO3, NH4, SIL, DON, PON, OPL)_{SKL} \times IMR.$$

According to this formulation, the concentration of all biogeochemical variables in the sea ice component decreases to zero when sea ice entirely disappears due to the melting process in each model grid. Although sea ice melts from its surface, bottom, and flank, respectively, it is difficult to separate these melting processes in terms of particle export. In general, ice surface meltwater sinks through internal brine channels and flushes out a part of materials in the skeletal layer (Vancoppenolle et al., 2010). Besides, ice algae have an ability to maintain their

position under a slow melting rate, and the habitat is not immediately lost even after ice bottom melting. The methods adopted in the present work idealize ice-ocean exchange of biogeochemical variables within reasonable scopes.

The nutrient source of ice algal growth can be divided to the sea ice column and underlying seawater. The present study assumes that ice algae utilize both ice/ocean nutrients depending on their biomass:

$$N_{up} = RN_{upSKL} \times N_{upSKL} + (1 - RN_{upSKL}) \times N_{upOCN},$$

$$RN_{upSKL} = 0.5 \times \{ \cos(\pi \times IA / KN_{upSKL}) + 1 \}, \text{ for } IA \leqq KN_{upSKL},$$

where RN_{upSKL} is the ice algal uptake ratio of nutrient in the skeletal layer, and KN_{upSKL} is a threshold value (Fig. 3c). When ice algal biomass IA exceeds $KN_{upSKL,}$ only seawater nutrients are utilized for the growth. The value of KN_{upSKL} is set to 1 mmol N m^{-2} in the present experiments. As reported in Section 3.2, sea ice nutrients are consumed preferentially for the initial bloom of small-sized ice algae in early summer. According to the growth of ice algae, their nutrient source shifts to seawater for the mature period. The "hybrid-type" formulation of nutrient uptake represents more realistic ice algal biology, where ice algae anchoring under ice floes gradually raise meter-long filaments in the water column (Boetius et al., 2013). In each model time step, the Michaelis-Menten relationship is applied to nutrient concentration in the skeletal layer and in the ocean surface layer (i.e., the uppermost ocean grid), respectively (Fig. 3d):

$$N_{upSKL} = \min\{ NO3_{SKL} / (NO3_{SKL} + K_{NO3}) \times \exp(-\Psi_{NH4} \times NH4_{SKL}) + NH4_{SKL} / (NH4_{SKL} + K_{NH4}), SIL_{SKL} / (SIL_{SKL} + K_{SIL}) \},$$

$$N_{upOCN} = \min\{ NO3_{OCN} / (NO3_{OCN} + K_{NO3}) \times \exp(-\Psi_{NH4} \times NH4_{OCN}) + NH4_{OCN} / (NH4_{OCN} + K_{NH4}), SIL_{OCN} / (SIL_{OCN} + K_{SIL}) \},$$

where the constant coefficients of half saturation for nitrate (K_{NO3}), ammonium (K_{NH4}), and silicate (K_{SIL}) and of ammonium inhibition (Ψ_{NH4}) have the same values (Table 1) as those of pelagic diatoms (i.e., large phytoplankton PL in the NEMURO model) (Kishi et al., 2007).

The ice algal biomass decreases due to mortality, grazing, and sea ice melting. The respiration and mortality terms are functions of the ice algal biomass itself (under the freezing temperature assumption). In the present experiments, there is no biomass of ice-related fauna, and the grazing pressure on ice algae is neglected except for a sensitivity experiment in Section 5.4. All ice algae are included in ice-derived PON without any biological activities after their export into the water column by melting sea ice. Sea ice assemblages sink faster than other particles derived from pelagic plankton because ice algae aggregate before the release from the sea ice bottom. Boetius et al. (2013) indicated rapid sinking of ice-related species. Hence, the modeled PON is divided into two components with different sinking speeds. The sinking speeds of PON derived from ice algae (pelagic plankton) are from 50–200 m d^{-1} (2–200 m d^{-1}), following a cosine curve (Fig. 3e). The sinking speed is maintained at 200 m d^{-1} below a depth of 1,000 m. These profiles are reasonable, because sinking of particulate organic materials generally accelerates with depth due to particle densification processes (e.g., aggregation in shallow depths and elimination of light/fragile organic materials at middle depths) (Honda et al., 2013). The modeled OPL is treated in the same manner. We refer to the fast- and slow-sinking PON/OPL as fPON/fOPL and sPON/sOPL, respectively.

The horizontal advection of biogeochemical variables in the sea ice component is also calculated, as the Arctic NEMURO is implemented in a three-dimensional framework. The divergence (convergence) of sea ice velocity causes loss (accumulation) of each material as well as snow and ice volumes. The actual ridging process is accompanied by complex

deformation, whereas the modeled sea ice ecosystem is kept consistently in the skeletal layer with a constant 2-cm thickness for simplicity.

2.3 Experimental design

The model domain contains the entire Arctic Ocean, the Greenland-Iceland-Norwegian Seas, and the northern part of the North Atlantic (Fig. 1). The horizontal resolution is 5 km, and there are 1,400 × 1,000 grids. There are 42 hybrid σ-z vertical levels. Vertical resolution varies from 2 m at the top to 500 m at the bottom. The σ-coordinate composed of three levels is applied to the uppermost 10 m. We performed two one-year experiments (called the 2011 and 2012 cases), in which the 5-km grid model was integrated from October 2010 (2011) to September 2011 (2012) to examine seasonal and interannual variability in ice algae. The initial sea ice and ocean physical fields for these experiments were obtained from a 1979–2011 decadal experiment using the 25-km grid version (Onodera et al., 2015). The atmospheric forcing components were constructed from the National Centers for Environmental Prediction/Climate Forecast System Reanalysis (NCEP/CFSR) 6-hourly dataset (Saha et al., 2010). Pacific water inflow is provided at the Bering Strait, based on Woodgate et al. (2005). Following our previous modeling study (e.g., Watanabe, 2011), the idealized seasonal cycles of northward velocity, temperature, and salinity are prescribed such that the annual mean inflow is 0.8 Sv (1 Sv ≡ 10^6 m^3 s^{-1}) and temperature (salinity) reaches a maximum in September (March). Monthly nitrate and silicate concentrations derived from the World Ocean Atlas 2013 (Garcia et al., 2013) are used for a restoring along the lateral boundary region of the model domain, and summer climatology is assigned to the initial fields of ocean nutrients. As PON and opal in sea bottom sediments are crucial nutrient sources for the Arctic shelves via decomposition and remineralization processes,

the fluxes in ammonium, DON, and silicate are added to the deepest layers just above the shelf bottom as in Watanabe et al. (2014). Sea ice nutrients are initially non-existent in the skeletal layer, and the lowest ice algal concentration of 0.02 mmol N m^{-3} is given for initial growth (i.e., seeding). The relationship of 1 mmol N = 80 mgC = 1.6 mgChl is assumed using a C/Chl mass ratio of 50 and a C/N Redfield ratio of 6.625 to compare the model outputs with observational estimates, as in Watanabe et al. (2012).

2.4 Sediment trap analysis

The bottom-tethered sediment traps (SMD26S-6000, NiGK Cooperation) have been moored at Station NAP (75°N, 162°W, 1,975-m water depth) since October 2010. Deployment and turnaround were conducted by the Japanese R/V Mirai and the Canadian Coast Guard Ship Sir Wilfrid Laurier. Sinking particles were sampled at depths of 181–218 m (median, 184 m) during the first year from October 4, 2010 to September 27, 2011. The trap depth was 247–319 m (median, 256 m) during the second year from October 4, 2011 to September 17, 2012. These sediment traps collected 26 samples approximately every two weeks during their one-year deployment. The recovered trap samples were sieved through 1-mm mesh to remove swimmers, and particles < 1 mm were divided evenly into 10 sub-samples. One of 10 aliquot samples was filtered, and was desalted using Milli-W water. The dried sample was weighed, and it was then ground and mixed using an agate mill. PON and POC contents were analyzed in one sequence. The powdered samples were decalcified in hydrochloric acid vapor in a desiccator for eight hours to remove particulate inorganic carbon. Sodium hydroxide pellets were placed in the desiccator to neutralize the samples. PON content in the treated samples was sequentially analyzed by a CHN analyzer (NCS2500, Thermo Quest). Sinking PON flux was calculated based on PON content, sampling period, open area of the sediment trap (0.5 m^2), and aliquot

297 size of the treated sample (1/10). The detailed analysis method and diatom valve fluxes were
298 described in Onodera et al. (2015). The structures of radiolarians and copepods captured in the
299 same traps were reported in Ikenoue et al. (2015) and Matsuno et al. (2015), respectively.
300

3. Seasonal transition in the Chukchi Borderland

3.1 Physical environments

We defined the NAP region as that enclosed by 74°–76°N and 159°–165°W for the following analyses (Fig. 1). Monthly mean values of the NCEP/CFSR cloud fraction, downward shortwave radiation, wind speed at a height of 10 m, snow depth, sea ice thickness, and sea ice concentration averaged in the NAP region are summarized in Table 2. The modeled physical variables were checked (Fig. 4). The NAP region was entirely covered by sea ice during the winter and spring seasons from December to April, and sea ice concentration decreased gradually from May to September in both the 2011 and 2012 cases (Fig. 4a). The area-mean sea ice thickness reached approximately 200 cm in April (Fig. 4b), which was a typical value north of the Chukchi Sea (Haas et al., 2010). The declines in sea ice concentration and thickness were consistent with the sea ice melting period from May to September (Fig. 4c). The mechanical divergence of sea ice flow fluctuated within the range of ± 0.2 d^{-1} in early winter and late summer (Fig. 4d).

Compared with the sea ice conditions simulated in the 2011 case, the early-winter covering of sea ice was somewhat delayed in the 2012 case. Although sea ice continued to melt until mid-November, winter sea ice thickness was greater in the 2012 case. The anomalous wind pattern could account for thicker ice transport toward the NAP region, as suggested in Section 4.1. The negative anomaly of sea ice thickness in the 2011 case was additionally caused by two melting events in November and December (Fig. 4c) and the blanket effect of more snow accumulation on top of the sea ice (not shown). The faster rate of sea ice decline caused earlier sea ice opening in the 2012 case (Figs. 4a-b), partly due to lower surface albedo from less snow cover. These snow and sea ice differences were compatible with the NCEP/CFSR data (Table 2).

In addition, the enhanced mechanical divergence of sea ice flow from mid-July to August accelerated the sea ice reduction in 2012 (Fig. 4d). Ice algal biomass in a specific region can change based on sea ice divergence events. The detailed processes associated with cyclone activities are discussed in Section 4.4.

As ice algal primary production depends highly on nutrient conditions in the underlying ocean surface layer, replenishment of nitrate and silicate from depths in the nutricline is substantially important. The Ekman upwelling and downwelling velocities were calculated from the modeled ocean surface stress fields (i.e., the combination of wind stress in open water area and ice-ocean stress under sea ice). The week-long Ekman downwelling occurred in both cases during the winter, as usually seen inside the Beaufort Sea (Yang, 2009), and a strong upwelling event appeared in the 2011 case (Fig. 4e). In July–August, the Ekman velocity sign was opposite between the two cases. The mid-summer Ekman downwelling (upwelling) played a role in the nutricline deepening (shoaling) in the 2011 (2012) case. The vertical turbulent mixing was characterized by vertical diffusivity diagnosed using the closure scheme of Noh and Kim (1999) in the present model. Turbulent mixing was activated during winter in the 2011 case (Fig. 4f). During the other periods, the smaller values of modeled vertical diffusivity by one or two orders indicated that the mixing process had a relatively minor impact on nutrient entrainment in the NAP region.

343 **3.2 Ice algal production**

344 The modeled ice algal production demonstrated remarkable spatial and interannual
345 variability in the western Arctic Ocean (Fig. 5). Annual production exceeded 0.6 mmol N m^{-2}
346 over most of the Chukchi Sea shelf, whereas low productivity < 0.1 mmol N m^{-2} was located in
347 the central Canada Basin. The shelf-basin contrast in ice algal production was previously
348 detected by the trans-Arctic Ocean expedition in the 1990s (Gosselin et al., 1997) and
349 represented by decadal model simulations (Jin et al., 2012; Dupont, 2012). In the 2011 case, the
350 local maximum appeared north of the Chukchi and Beaufort shelf breaks (Fig. 5a), whereas ice
351 algal productivity was suppressed considerably around the Beaufort Gyre region in the 2012
352 case (Fig. 5b). The negative anomaly widely covered the western Arctic except the coastal
353 shelves and the northern part of Chukchi Borderland (Fig. 5c). Station NAP was located near
354 the shelf-basin boundary and also showed the negative anomaly.

355 In the NAP region, the modeled ice algal bloom started in June and produced a peak
356 biomass of 0.7 mmol N m^{-2} at the beginning of August in the 2011 case (Fig. 6a). The peak
357 timing was a few months later than the pan-Arctic averages simulated in previous models (Jin
358 et al., 2012; Deal et al., 2011), partly because the NAP region is located north of highly
359 productive shelves. An additional reason for the lagged peak phase may be attributed to a lower
360 photosynthetic response to incoming solar irradiance in the present model setting. Sensitivity to
361 optimum light intensity is shown in Section 5.1. The Hovmöller diagram visualized the vivid
362 shelf-basin contrast along the 75°N line (Fig. 6b). The bloom signal was quite weak inside the
363 Canada Basin. A massive ice algal bloom up to 10 mmol N m^{-2} was simulated in July over the
364 Chukchi northern shelf to the west of the NAP region. The modeled ice algal biomass north of
365 the Chukchi Sea was within the lower range of 1–340 mgChl m^{-2} in Arctic sea ice (Arrigo et al.,

366 2010) and an order of magnitude smaller than that measured in Resolute Passage (160 mgChl
367 m^{-2}; Michel et al., 1996). The Chukchi Borderland has shifted from a perennial ice-covered area
368 to a seasonal ice zone in recent years. Multi-year ice would have dimmed the ice algal bloom
369 until the past decades in this area. It is also reasonable that substantially less amounts of
370 nutrients restricted ice algal growth to the level below the pan-Arctic averages. In the 2012 case,
371 initial bloom timing was further delayed by one month and ice algal biomass was clearly
372 smaller than that of the 2011 case (Figs. 6a, c).

373 As introduced in Section 2.2, ice algal production rate was calculated using the empirical
374 functions of light condition and nutrient uptake terms. The light condition in the skeletal layer
375 of the sea ice column was recovered slowly after the end of polar night (February in the NAP
376 region) and then increased rapidly due to thinning of snow/ice in May (Fig. 7a). Peak values of
377 PAR (3.5 W m^{-2} in the 2011 case, and 2.2 W m^{-2} in the 2012 case) were recorded in mid-July
378 after the summer solstice. Although sea ice melting continued until September, light intensity
379 turned to decrease in accordance with the annual cycle of solar radiation. As the optimal light
380 intensity for ice algal growth (I_{opti}) was set to 10 W m^{-2} in the present experiments, the light
381 condition term varied in phase with the PAR transition (Fig. 7b). The weaker summer light
382 intensity in the 2012 case could be attributed to the depressed shortwave radiation due to more
383 cloud cover (Table 2), despite thinner sea ice in August (Fig. 4b). The cyclone impact on light
384 conditions is described in Section 4.4.

385 The nutrient conditions in the sea ice and water columns showed remarkable interannual
386 variability. Sea ice nitrate content peaked at 0.6 mmol N m^{-2} (0.2 mmol N m^{-2}) in the 2011
387 (2012) case (Fig. 8a), which was an order of magnitude smaller than in landfast ice in Resolute
388 Passage of the Canadian Archipelago (Cota and Smith, 1991). Potential factors contributing to

389 the difference include the nutrient environment in the underlying water column and the sea ice
390 freezing rate, because nutrient accumulation in the skeletal layer was induced by ocean-to-ice
391 flux during the sea ice freezing period (see formulation in Section 2.2). At the beginning period
392 of the one-year model integration, the nutricline depth was located at 20 m in the NAP region
393 (Figs. 8b-c). Ekman downwelling helped deepen the nutricline from October to early November
394 in both cases (Fig. 4e). In the 2011 case, Ekman upwelling was also evident in November.
395 However, the duration was just one week, so the Ekman contribution with a peak of 0.8 m d^{-1}
396 played a minor role in nutrient entrainment. The more important contributory process was
397 strong mixing during winter in the 2011 case, as shown by the enhanced vertical diffusivity (Fig.
398 4f). According to these processes, the surface nitrate concentration reached 2 mmol N m^{-3} (Fig.
399 8b), and a significant part was imported into the skeletal layer (Fig. 8a). In contrast, the
400 oligotrophic water stayed over the nutricline, which was at a nearly constant depth or somewhat
401 deepened during winter in the 2012 case (Fig. 8c). Sea ice nitrate content reflected the ocean
402 surface value of < 1 mmol N m^{-3}. Sea ice silicate, which had a similar difference to nitrate, was
403 not a limiting factor for ice algal growth in the NAP region (not shown). The rate of sea ice
404 freezing also differed between the two cases. The total amount of thermal sea ice growth from
405 October to April was 160 (136) cm in the 2011 (2012) cases. Whereas we focused on the
406 seasonal transitions from winter to early summer, *in-situ* data of nutrient concentration and sea
407 ice freezing rate were unavailable for the target region and period. Accordingly, proper
408 evaluations of the modeled properties, particularly during winter, were difficult at this stage. At
409 least, the model results suggest that preconditioning of nutrient accumulation in the sea ice
410 column during the freezing period controlled the interannual variability in the ice algal bloom.

411 The influences of the basin-scale wind pattern and water mass transport on the nutrient
412 environment are analyzed in Section 4.

413 Nutrient availability for ice algal production reflected the difference in this preconditioning.
414 Based on the present model formulation, sea ice nutrients were consumed primarily during an
415 initial stage of the ice algal bloom, and nutrients in the ocean surface layer were utilized for
416 further blooms. According to ice algal growth (Fig. 6a), the uptake ratio of sea ice nutrients
417 (RN_{upSKL}) shifted from 1 to 0.7 within a few weeks of July in the 2011 case (Fig. 7c). When the
418 half-saturation constant for nitrate uptake (K_{NO3}) was set to 6 mmol N m^{-3} for ice algae as well
419 as pelagic diatoms (PL in the present model), the nitrate uptake term before the ice algal bloom
420 was approximately 0.9 (0.7) in the 2011 (2012) case (Fig. 7d). The growth ratio between the
421 two cases became 1.8 at the beginning of June after multiplying the light condition term (Fig.
422 7b). The larger growth rate accounted for the earlier initial ice algal bloom in the 2011 case (Fig.
423 6a). Sea ice nitrate was depleted rapidly by this initial bloom and partially by export to the
424 water column with melting sea ice (Fig. 8a). The subsequent decrease in the RN_{upSKL} value
425 represented utilization of the underlying seawater nutrients (Fig. 7c). The additional bloom
426 occurred in late July (Fig. 6a). In the 2012 case, the decrease in the nutrient uptake term lagged
427 behind the 2011 case in accordance with the delay of the initial bloom (Fig. 7d). The ocean
428 nutrient uptake term, which had lower values during the ice freezing period, gradually became
429 comparable with the 2011 case. However, the higher RN_{upSKL} value, except in early August,
430 restricted ocean nutrient uptake in the 2012 case (Fig. 7c).

431 As expected, the seasonal transition of the ice algal biomass was similar to daily primary
432 productivity (Figs. 9a-b). In the present model experiments, primary production derived from
433 nutrients in the skeletal layer and in the water column was calculated separately. In the 2011

434 case, the nutrient source for the ice algal bloom changed from the sea ice column for the first
435 primary production peak of 23 μmol N m^{-2} d^{-1} to seawater for the second larger peak of 82 μmol
436 N m^{-2} d^{-1}. The second peak value of ~ 6.6 mgC m^{-2} d^{-1} was close to the field-based estimates of
437 4–9 mgC m^{-2} d^{-1} on the Beaufort shelf and slopes (Gradinger, 2009) and < 10 mgC m^{-2} d^{-1} in
438 the Arctic basins (Deal et al., 2011). The model results indicate that nutrients imported in the
439 sea ice column determine the beginning of the ice algal bloom, and that ocean nutrients have a
440 greater contribution to annual ice algal production, as reported previously (Gradinger, 2009).
441 The comparison with the PON export to the underlying water column suggested that more than
442 half of the organic nitrogen was remineralized in the sea ice column (Fig. 9a). In the 2012 case,
443 the peak of primary production simulated in early August was 35 μmol N m^{-2} d^{-1} (Fig. 9b). The
444 relative contribution of ocean nutrients to primary productivity was less than that in the 2011
445 case. The August peak in PON export flux exceeding ice algal productivity was attributed to
446 lateral advection of shelf-origin sea ice floes. The detailed discussions are presented in Section
447 4.3 and 4.4.
448

4. Wind-driven dynamics associated with ice algal productivity

To examine background mechanisms for year-to-year changes in ice algal productivity, wind-driven sea ice and ocean dynamics in the western Arctic Ocean were addressed.

4.1 Wind and sea ice patterns

Interannual variabilities in sea ice motion and ocean surface currents in the Beaufort Sea are closely related to the atmospheric circulation pattern (Yang, 2009; Proshutinsky et al., 2009). We compared the winter mean sea level pressure (SLP) and wind stress fields constructed from the NCEP/CFSR reanalysis data between the two years. Wind stress was calculated from the daily mean SLP using a protocol of the Arctic Ocean Model Intercomparison Project (AOMIP) (http://www.whoi.edu/page.do?pid=30576). An anti-cyclonic wind pattern was accompanied by a weak Beaufort High around the Canada Basin during winter 2010–2011 (Fig. 10a). The easterly wind in the southern Beaufort Sea was favorable for transporting Chukchi shelf water toward the southern Canada Basin and the NAP region via the Ekman process. Ekman transport was analytically estimated with a seawater density of 1.025×10^3 kg m^{-3} and a Coriolis coefficient of 1.4×10^{-4} s^{-1}. A sea ice-ocean stress value of 0.1 Pa, which was frequently recorded along the Chukchi shelf break during early winter in the 2011 case, yielded an Ekman transport value of 0.7 m^2 s^{-1} (1.8 km^2 mon^{-1}). This value is close to the November climatology in the southern Beaufort Sea (Yang, 2009) and indicates a shelf-basin water exchange of 900 km^3 mon^{-1} for a shelf break axis length of 500 km. In contrast, high SLP extended from the Siberian Arctic to the western Arctic Ocean in winter 2011–2012 (Fig. 10b). Accordingly, a northwesterly wind prevailed in the Beaufort Sea. In this situation, no definite shelf water transport toward the NAP region was expected by the winter wind fields.

472 The changes in wind patterns were consistent with the modeled physical environments in
473 the NAP region, where several differences between the 2011 and 2012 cases were described in
474 Section 3.1. For October to early November 2011 (i.e., the beginning period of in the 2012
475 case), localized anti-cyclonic wind forcing was closely related to the modeled negative rate of
476 sea ice growth, convergence of sea ice velocity, and Ekman downwelling in the NAP region
477 (Figs. 4c-e). The wind-driven warm water intrusion toward the marginal ice zone induced
478 lateral/bottom melting of sea ice floes (not shown). The convergence in sea ice velocity
479 increased sea ice thickness via mechanical ridging processes, in contrast to sea ice melting
480 occurring during the same period. The continuous Ekman downwelling was also accompanied
481 by the sea ice convergence. For the period afterwards, the positive anomaly of sea ice thickness
482 was produced by southward transport of thicker sea ice from the central Arctic in the 2012 case
483 (Fig. 4b). The direction of sea ice flow around the NAP region clearly differed between the two
484 years (Figs. 10c-f), as detected previously by satellite-based and modeled spatial patterns
485 (Onodera et al., 2015). Both the daily time series in the Polar Pathfinder sea ice motion vectors
486 (Fowler et al., 2013) and in the simulation results showed the successive southward advection
487 of sea ice from late October 2011 to January 2012 (Figs. 10d, f). The distance of sea ice
488 movement reached several hundred km during this period when sea ice velocity was 5 cm s^{-1}
489 (ca. 130 km mon^{-1}). These results suggest that the anomalous wind pattern forced southward
490 transport of oligotrophic sea ice and water masses within the Beaufort Gyre and eventually
491 lessened nutrient availability in the Chukchi Borderland.
492
493 **4.2 Nutrient and shelf-break tracer distributions**
494 The nutrient preconditioning that occurred before the ice algal blooming period reflected
495 the wind-driven sea ice and water mass transport, as suggested in Section 4.1. The spatial

496 distribution of the ocean nitrate concentration was characterized by a sharp meridional gradient
497 across the Chukchi and Beaufort shelf breaks (Figs. 11a-b), as captured by a number of ship-
498 based observations (e.g., Nishino et al., 2011). The modeled vertical average in the top 30 m
499 reached 10 mmol N m^{-3} in the central Chukchi Sea and was < 1 mmol N m^{-3} in the Canada
500 Basin. As shown in Fig. 8, nitrate content around the NAP region tended to differ. In the 2011
501 case, relatively high nitrate concentrations were distributed from the northern shelf of the
502 Chukchi Sea to east of Northwind Ridge along 75°N (Fig. 11a). On the other hand, the shelf-
503 basin contrast in nitrate content was still apparent even in the southern area of Chukchi
504 Borderland in the 2012 case (Fig. 11b).

505 To explore the paths of the shelf-break water, a virtual passive tracer was provided along
506 the shelf-basin boundary. We chose the tracer source region sandwiched by the 100–200-m
507 isobaths. The tracer value was fixed continuously to one (i.e., 100% concentration) at depths of
508 0–200 m in the defined region through each one-year experiment. Advection and diffusion of
509 the tracer in the other regions were calculated as well as seawater temperature and salinity. The
510 modeled distribution in March 2011 indicated that the tracer provided along the shelf-basin
511 boundary region was transported from the Chukchi northern shelf toward the interior of the
512 Canada Basin. The northern edge of the tracer matched the nitrate-rich area in the 2011 case
513 (Fig. 11a). The vertical profile of nitrate concentration in the NAP region reflected the
514 deepening nutricline driven by the Ekman downwelling in October (Figs. 4e and 11c).
515 Subsequently, nitrate content in the upper 50 m showed a net increase during December–
516 January, which could be explained by lateral input rather than local vertical mixing. Hence, the
517 model results indicate that Ekman transport of Chukchi shelf water along with energetic
518 turbulent mixing enhanced nutrient availability for ice algae in the NAP region. In contrast, in

519 March 2012, the tracer signal was quite weak over the Chukchi Borderland (Fig. 11b). No
520 significant change appeared in the vertical nitrate profile during winter after the wind-driven
521 downward shift (Fig. 11d). The spread of fresher basin water blocked the intrusion of shelf
522 water and weakened the turbulent mixing. The density stratification plausibly controlled ocean
523 subsurface mixing, as wind speed averaged from November to January of the 2011 and 2012
524 winter periods was comparable (Table 2). This mechanism was consistent with previous
525 findings, in which the mixed layer depth correlated with hydrographic structures rather than
526 wind forcing in the western Arctic (Peralta-Ferriz et al., 2015).

527 Onodera et al. (2015) categorized the sinking diatom assemblages in the sediment trap
528 samples at Station NAP into 98 taxa. The dominant species during summer 2011 were *Fossula*
529 *arctica* and the *Fragilariopsis* group (*F. cylindrus* and *F. oceanica*), which are common in ice
530 algae in the shelf region (Cremer, 1999). Their relative abundances were minor in the sinking
531 diatom flora during summer 2012. Instead, the major diatom in August 2012 was planktic
532 species such as *Thalassionema nitzschioides*, which was commonly observed in the Canada
533 Basin. In addition, the sinking flux of total diatom valves in August 2012 was considerably
534 lower than that in August 2011. The observed diatom compositions and valve fluxes were
535 consistent with the above-mentioned physical backgrounds. The modeled nitrate distribution
536 and tracer pathway supported the suggestion that winter transport of oligotrophic water from
537 the interior of the Canada Basin toward the NAP region was an important factor suppressing ice
538 algal productivity during summer 2012.
539
540 **4.3 PON flux**
541 The time series of sinking PON flux in the NAP region was compared with the sediment
542 trap data. The modeled PON flux at 180 m in the 2011 case increased gradually from June and

543 peaked at 18 μmol N m^{-2} d^{-1} in mid-August following the ice algal bloom (Fig. 9c). Flux > 8
544 μmol N m^{-2} d^{-1} continued until the end of the model integration (i.e., September). The flux
545 amount was underestimated in August and became comparable afterward with the trap values.
546 PON flux at 180 m corresponded to 79% of the ocean surface value exported from the sea ice
547 bottom during July–September 2011 (Figs. 9a, c). It should be noted that ice algae released
548 from the skeletal layer were included immediately in the ice-derived PON without being
549 suspended and seeding in the present model setting. The major component of PON flux
550 originating from ice algae, as observed in the analysis of diatom valve compositions (Onodera
551 et al., 2015). PON flux derived from pelagic phytoplankton and zooplankton increased
552 gradually in August and peaked at 6 μmol N m^{-2} d^{-1} in early September (Fig. 9c). In the 2011
553 case, the dominance of the ice-derived PON for the sinking flux was associated with its faster
554 sinking speed (Section 2.2 and Fig. 3e), although the total biomass of pelagic plankton groups
555 was an order of magnitude larger than that of the ice algal biomass (not shown). The sediment
556 trap data captured another peak in PON flux during May 2011, when the model experiment
557 could not reproduce the peak. Neither spring bloom of ice algae nor pelagic phytoplankton was
558 expected due to the thick ice cover in the NAP region (Fig. 4b and Table 2). This event may
559 have been caused by transport of shelf water with lithogenic materials of sea bottom sediment.
560 A candidate driver was a cold-core eddy generated from a narrow jet along the Chukchi shelf
561 break (Spall et al., 2008; Llinás et al., 2009). The background mechanisms for the spring peak
562 are beyond the scope in the present study and will be analyzed in the future.

563 PON flux in the 2012 case produced a distinct mid-summer peak at the ocean surface and
564 at 180 m, although the trapped sample volume was too low to estimate nitrogen content in
565 summer 2012 (Fig. 9b, d). The trap depth of 247–319 m in 2012, which was deeper than that of

181–218 m in 2011, may have caused biases in the comparison between the two years. Importantly, PON flux in 2012 was markedly lower than the 1,300-m flux in 2011 (Onodera et al., 2015). Again, most of the modeled PON flux was ice-derived. The contribution of pelagic-derived PON in the 2012 case was rather less than in the 2011 case. Enhanced sea ice melting of up to 4 cm d^{-1} assisted the peak flux in early August (Fig. 4c). The ice-ocean flux was remarkably greater than the ice algal production rate, indicating that one-dimensional sea ice processes cannot account for PON flux in the NAP region (Figs. 9b). We trace lateral advection of the ice algal biomass around the Chukchi Borderland in the next section.

4.4 Impact of great cyclone activity

It was suggested that an extreme cyclone event was a supplementary factor for the drastic sea ice reduction, particularly in the western Arctic, and the subsequent record minimum extent of Arctic sea ice in summer 2012 (Simmonds and Rudeva, 2012; Zhang et al., 2013). A previous modeling analysis indicated that plankton productivity over the Chukchi, East Siberian, and Laptev shelves was enhanced by vertical mixing with nutrient replenishment and lateral plankton transport of from the western Arctic basin during the cyclone storm (Zhang et al., 2014). It is assumed that synoptic cyclone activities have both positive and negative contributions to ice algal production. In the 2012 case, the event-like shoaling of the upper part of the nutricline was caused by mixing and upwelling processes in the NAP region, where the southern part of the great cyclone passed and marginal ice floes were located in early August (Fig. 12a). The modeled vertical diffusivity was maintained at background values partly because strong density stratification suppressed turbulent mixing until July 2012 (Fig. 4f). During the cyclone event with high wind speeds (Table 2), vertical mixing of nearly 10 cm^2 s^{-1} reached a depth of 20 m (Figs. 4f). Besides, the Ekman upwelling that continued from July 15

590 to August 29 could have worked on nutricline shoaling of 3.3 m (Fig. 4e). However, this timing
591 of nutrient replenishment overlapped with the release of ice algae from the skeletal layer due to
592 active sea ice melting (Fig. 8c), and the mixing and upwelling processes hardly enhanced ice
593 algal productivity. Mechanical sea ice divergence associated with cyclonic wind fields rather
594 contributed to the reduction in ice algal biomass in the specific region (Fig. 4d). Whereas the
595 outward movement of sea ice floes itself did not lead to loss of ice algae, solar heat absorption
596 into the exposed open water fractions enhanced lateral/bottom melting of sea ice and
597 corresponding release of ice algae. The light conditions for ice algal growth also changed by
598 during the cyclone event with extensive cloud cover. The NCEP/CFSR reanalysis data showed
599 a depression in solar irradiance in the southern part of the cyclone passage, where an early
600 August shortwave flux in 2012 was lower than that in 2011 by approximately 20 W m^{-2} (not
601 shown). The negative anomaly of light intensity corresponded to a decrease in the light
602 condition term for ice algal growth by less than 0.1.

603 Here, we performed a sensitivity experiment in which all biogeochemical processes in the
604 sea ice ecosystem were halted in August 2012. In this idealized experiment (called the “no ice
605 algal activity case”), only lateral advection and sea ice-ocean fluxes were allowed in the sea ice
606 column. All physical and pelagic marine ecosystem processes were calculated as in the original
607 2012 case. Although there was no ice algal production in August, both the modeled ice algal
608 biomass and PON flux increased in the NAP region (Figs. 12c-d). These enhanced signals could
609 only be explained by horizontal transport of larger biomass from neighboring regions. The
610 differences from the original case corresponded to additional production of ice algae flowing
611 into the NAP region. Thus, lateral advection was essentially important during the 2012 cyclone
612 period.

613 In the 2012 case, westerly winds were intensified in the southern part of a cyclone passage
614 and transported shelf-origin ice algal patches toward the Northwind Ridge. Each sea ice floe
615 moved approximately 150 km eastward during August 3–10 (Fig. 12b). Although the direction
616 of sea ice motion (87.4°T) was similar to the satellite-based vectors (82.8°T), the modeled drift
617 speed (20.3 cm s^{-1}) was markedly faster than the latter (5.1 cm s^{-1}) during the cyclone period. It
618 is plausible that the peculiar advection caused a sudden increase in ice algal biomass and an
619 overestimation of the modeled PON flux in the NAP region (Figs. 6a and 12b). Local biases on
620 sea ice velocity may have arisen from atmospheric momentum input and sea ice dynamics. In
621 the present experiments, the conversion from SLP to the wind stress field (i.e., the AOMIP
622 protocol referred to in Section 4.1) was formulated with specific turning angles, which varied
623 depending on geostrophic wind speed (Proshutinsky and Johnson, 1997). Uncertainties in the
624 reanalysis SLP data should also be considered, because the maximum strength of the great
625 cyclone in August 2012 calculated from the data assimilation system depended on the number
626 of radiosonde profiles (Yamazaki et al., 2015). In addition, the traditional rheology of sea ice
627 internal stress has been developed for climate models with grid spacing much coarser than 10
628 km and does not guarantee the accuracy of ice floe dynamics, especially in the marginal ice
629 zone. Thus, speed and direction of the modeled ice algal advection around the Chukchi
630 Borderland may have deviated in August 2012. These biases had less impact on the basin-scale
631 sea ice and ocean circulation.

632 Another concern is the event-like deepening of the shallow sediment trap at Station NAP in
633 July 2012 (Onodera et al., 2015). An intensified ocean current occasionally inclines the upper
634 part of the bottom-tethered mooring system during storms. The anchored sea bottom depth of
635 1,975 m and deepening of the trap from 260 to 320 m suggests an inclination angle of

636 approximately 15°. It was reported that trapping efficiency and particle components were
637 remarkably influenced by tilting > 30° (Gardner, 1985). If this previous examination can be
638 applied despite the different trap shape, a 15° tilt should not significantly impact trapping
639 efficiency. In addition, strong ocean currents > 10 cm s^{-1} sometimes reduce trapping efficiency
640 (Baker et al., 1988). However, the modeled horizontal velocity at the trap depths was below 2
641 cm s^{-1}, even during the cyclone period (not shown). It should also be noted that the trapped
642 PON flux was continuously negligible throughout summer 2012, not only for the temporal
643 cyclone event.
644

5. Sensitivity experiments

Although the present model experiments show the interannual variability in ice algal primary production and sinking biogenic particle flux in the NAP region, various sea ice-related processes still need to be considered. Here, we refer to the 2011 case analyzed in previous sections as the original case and performed sensitivity experiments using different model settings (Fig. 13). The first three cases (Cases 1–3) address uncertainties in the model parameters. In the next three cases (Cases 4–6), the grazing pressure on ice algae and the treatments of ice algae released into the water column are discussed. All the sensitivity experiments were initiated from the modeled fields at the beginning of March in the original case for the saving of computational resources and conducted until September (i.e., seven months integration).

5.1 Optimum light intensity for ice algal production (Case 1)

It is difficult to estimate accurately the photosynthesis-irradiance relationships of ice-related flora. Ice algae adapt well to weaker light intensity compared with that of pelagic phytoplankton (Arrigo et al., 2010). In the original case, the optimum light intensity for ice algal production I_{opti} was set to 10 W m^{-2}. Gradinger (2009) reported that the minimum requirement for ice algal growth was typically < 1 μE m^{-2} s^{-1} based on laboratory incubation experiments. When the relationship of 1 W m^{-2} ~ 4.56 μE m^{-2} s^{-1} is applied following Lavoie et al. (2005), I_{opti} may be a smaller value. Here, we performed two sensitivity experiments with different I_{opti} values (Case 1). When I_{opti} was set to 5 W m^{-2} (20 W m^{-2}), the summer peak in the light condition term was 0.9 (0.3) in the NAP region (Figs. 3b and 7a). Relaxing the light limitation resulted in an earlier and stronger ice algal bloom (Fig. 14a). The initial bloom

668 occurred in early June and the second peak of ice algal biomass increased to 1.2 mmol N m^{-2} (cf.
669 0.7 mmol N m^{-2} in the original case). The phase and magnitude of the modeled PON flux
670 shifted similarly and were still comparable with the trap data (Fig. 14b). In contrast, restricted
671 light conditions dampened the ice algal productivity to a peak biomass of 0.1 mmol N m^{-2} (Fig.
672 14a). The resultant decreased release of ice algae into the water column delayed the seasonal
673 increase in the PON flux (Fig. 14b). The difference in ice algal biomass did not alter the flux
674 during late summer, which was derived mainly from pelagic plankton. Based on these
675 sensitivity experiments, an optimum light intensity of 10 W m^{-2} or below was recommended for
676 the formulation adopted. Other choices can be made for the light condition term. Ice algae may
677 not suffer from photo-inhibition even when the skeletal layer receives strong irradiance diffused
678 from neighboring open leads during ice melting periods. A saturated light condition in
679 accordance with increasing PAR can be represented, for example, by the hyperbolic tangent
680 function used in Lavoie et al. (2005). Besides, the shelf-shading effect of ice algae reduces ice
681 algal productivity in massive blooming regions (Pogson et al., 2011).
682
683 **5.2 Nutrient sources for ice algal production (Case 2)**
684 The present model adopted the hybrid nutrient uptake formulation. Ice algal productivity
685 depends on the uptake ratio between sea ice and water nutrients. Here, we performed three
686 experiments (Case 2). When the threshold value KN_{upSKL} is increased to 1.5 mmol N m^{-2}, (cf.
687 1.0 mmol N m^{-2} in the original case), the ice algal growth rate reflects nutrient availability in
688 the sea ice column more strongly (Fig. 3c). Conversely, the decrease in KN_{upSKL} to 0.5 mmol N
689 m^{-2} accelerates the uptake of seawater nutrients. However, the modeled ice algal biomass and
690 PON flux were not sensitive to this range of KN_{upSKL} (Figs. 14c-d). As in the original case (Figs.

691 7c and 9a), the major source of ice algal production was seawater nutrients, even when only
692 20% of the biomass could utilize (i.e., RN_{upSKL} = 0.8). On the other hand, both the ice algal
693 biomass and PON flux dropped remarkably in another experiment, in which uptake of sea ice
694 nutrients was halted throughout the integration period (Figs. 14c-d). The slower growth rate
695 with lower concentrations of seawater nutrients prevented ice algal seeds from blooming to the
696 same level as in the original case before sea ice melting loss (Fig. 7d). The nutrient reservoir
697 (and high concentration) in the sea ice column is important for the initial acceleration in an ice
698 algal bloom, and nutrient availability in the ocean surface layer controls peak biomass.
699 The exchange rate of dissolved materials at the ice-water interface generally depends on
700 molecular and turbulent diffusion processes. Lavoie et al. (2005) assumed that nutrient
701 replenishment from the underlying mixed layer was proportional to friction velocity varying
702 with the tidal cycle. The tidal effect is important in some regions such as the narrow straits of
703 the Canadian Archipelago. However, the essential improvement would be necessary for its
704 application to the entire Arctic Ocean. In this connection, the ocean-to-ice nutrient flux is
705 proportional to the CF_{OI} coefficient during the ice freezing period. A CF_{OI} value of 0 or 1 is
706 clearly unrealistic, because a significant portion of *in-situ* seawater nutrients remains inside the
707 sea ice column, and the residual is ejected to the underlying water column after sea ice freezing
708 as well as salinity. The original case adopted a CF_{OI} value of 0.3, following a first-year ice
709 salinity of ~ 10 psu. Smaller CF_{OI} values suppress nutrient accumulation in the skeletal layer
710 during the freezing period and delay the initial ice algal bloom. Another assumption in the
711 present model is that all of the sea ice nutrients are concentrated only in the skeletal layer with
712 its constant thickness (cf. 2 cm in the original case), instead of brine pockets and channels that
713 were not represented in the present model. An increase in the layer thickness reduces nutrient

714 “concentration” (not total amount integrated in the entire sea ice column) and consequently
715 delays an ice algal bloom. For example, a nitrate content of 0.6 mmol N m^{-2}, which was
716 recorded in April of the original 2011 case (Fig. 8a), yields a concentration of 30 mmol N m^{-3}
717 (12 mmol N m^{-3}) and a nitrate condition term of 0.91 (0.80) in the skeletal layer with 2-cm (5-
718 cm) thickness. A time-varying biologically active layer with brine volumes (Tedesco et al.,
719 2010) and multiple separate sea ice layers (Pogson et al., 2011) have been proposed to represent
720 ice algal habitats more precisely. These uncertainties in sea ice nutrients seem to have an impact
721 on ice algal production.
722
723 **5.3 Sinking speed of ice-derived PON (Case 3)**
724 The present model prescribed the fixed vertical profile of particle sinking speed (Fig. 3e).
725 In the original case, the sinking speed of ice-derived PON varied from 50 m d^{-1} in the
726 uppermost model layer to 200 m d^{-1} at a depth of 1,000 m. This speed range was comparable
727 with the previous estimate of > 85 m d^{-1} between the shallow (180 m) and deep (1,300 m) traps
728 at Station NAP in August 2011 (Onodera et al., 2015). The PON exported from the sea ice
729 bottom reached a depth of 180 m within four days under the model profile. As the
730 decomposition rate from PON to ammonium and DON was set to 0.2 d^{-1} at 0 °C, approximately
731 half (47%) of the ice-derived PON was dissolved above a depth of 180 m. Here, we performed
732 two experiments (Case 3), in which the minimum sinking speed was set to 200 (20) m d^{-1} in the
733 faster (slower) sinking case (cf. 50 m d^{-1} in the original case). The remaining ratio of ice-
734 derived PON after dissolution in these cases is theoretically 82% and 20% at a 180-m depth,
735 respectively. Sinking speed hardly affected ice algal biomass (Fig. 14e), although the vertical
736 nutrient profile in the water column had quite minor changes. On the other hand, PON flux

737 differed significantly between the two cases (Fig. 14f). The earlier and larger peak in the PON
738 flux appeared in the faster sinking case. The flux range obtained in Case 3 was smaller than the
739 sensitivity to the optimum light intensity evaluated in Case 1.

740 Actual sedimentation of biogenic particles depends on the ballast distribution in addition to
741 aggregation and elimination of light/fragile organic materials. When the source region of sea ice
742 and surface water in the NAP region was the central Canada Basin, an insufficient quantity of
743 ballast particles would have allowed slower PON sinking (Honjo et al., 2010). A variable
744 sinking speed depending ballast particles may improve a model performance on the PON flux.
745 Besides, the PON derived from phytoplankton and zooplankton possibly has a different sinking
746 speed. The faster sinking speed of fecal pellets may account for a substantial portion of the
747 particle flux as observed in Resolute Passage (Michel et al., 1996). Thus, many uncertainties
748 remain with respect to the PON sinking process.

749

750 **5.4 Grazing on ice algae (Case 4)**

751 Previous observations detected a significant quantity of ice-related fauna including
752 amphipods in the sea ice column (Bluhm et al., 2010). It was also reported that ice algal
753 assemblages suspended under the ice bottom layer were an important food source for pelagic
754 grazers (e.g., copepods) during the early stages of sea ice melting (Michel et al., 1996). Here,
755 the impact of the grazing process on ice algal biomass was examined (Fig. 13). In Case 4, the
756 concentration of ice-related fauna (IF) changed from zero in the original case (i.e., no grazing
757 pressure on ice algae throughout the integration period) to 0.02 mmol N m^{-3} on March 1. The
758 rate of IF grazing on ice algae was calculated following the Ivlev relationship:

759 $$Grz = \max\{0, Grz_{max} \times (1 - \exp\{\lambda (IA^* - IA)\})\},$$

where the maximum grazing rate Grz_{max} of 0.4 d^{-1} at 0 °C, the Ivlev constant λ of 1.4 (mmol N m^{-3})$^{-1}$, and the feeding threshold value IA* of 0.04 mmol N m^{-3} were given, as well as the grazing of mesozooplankton (ZL) on pelagic diatom (PL) in the original NEMURO model (Kishi et al., 2007). The Ivlev formulation assumes that no grazing occurs at an ice algal concentration IA lower than IA*. The modeled ice algal biomass showed the rapid decline after a similar peak compared with the original case (Fig. 4g). The ice-related fauna gradually increased following the ice algal bloom. A resultant peak of the IF biomass was 0.07 mmol N m^{-2}. This grazing process slightly contributed to the reduced PON flux (Fig. 14h). After sea ice melting, the released IF was included in ZL in the water column. For the sake of the enhanced grazing pressure in the water column, the phytoplankton biomass was also smaller than in the original case (not shown). We used same parameter values of the grazing process as pelagic planktons. When the skeletal layer is regarded as a refuge for ice algae from potential grazers, the maximum rate and consequent impact of grazing in the sea ice column should be smaller.

5.5 Transfer from ice algae to phytoplankton (Case 5)

It has been reported that a part of ice algae exported to the water column could continue their production activities as phytoplankton and become a zooplankton food source (Michel et al., 1993; Leventer, 2003; Gradinger et al., 2009). In Case 5, a constant ratio of ice algae released from the sea ice bottom was included in pelagic diatom (PL). The seeding partition was set to 0.5, assuming that a half of the released algae behaved in the form of living intact cells and the residual was included in the ice-related PON. Although the increased PL became a competitor of ice algae for the uptake of seawater nutrients in the uppermost ocean layer, the comparison with the original case showed little difference in the ice algal biomass (Figs. 14i).

On the other hand, the ice-derived algae staying alive in the water column were eventually included in the slower-sinking PON produced from pelagic species. These processes contributed to the decrease in PON flux at the trap depth (Fig. 14j). There is a wide uncertainty of seeding ratios of the released ice algae. For example, the ratio was set to 0.1 by Jin et al. (2012). To assess an impact of ice algal seeding to phytoplankton bloom and sinking biogenic fluxes more accurately, simultaneous measurements of diatom compositions both in the sea ice and water columns would be necessary.

5.6 Grazing on ice-derived PON (Case 6)

Zooplankton grazing on sinking biogenic particles could influence the quantity and composition of export fluxes in the water column. In Case 6, ZL grazing on ice-derived PON (fPON in the present model) was considered using the Ivlev equation:

$$Grz = \max\{0, Grz_{max} \times (1 - \exp\{\lambda (fPON^* - fPON)\})\},$$

where Grz_{max} of 0.4 d^{-1} and λ of 1.4 (mmol N m^{-3})$^{-1}$ were given as well as Case 4. The feeding threshold value fPON* was set to zero, and the contributions of other potential grazers (ZS and ZP in the present model) were neglected, for simplicity. This type of grazing hardly affected the ice algal biomass as in Case 3 (Fig. 14k), and the PON flux also showed little difference from the original case (Fig. 14l). A fPON concentration of 0.5 μmol N m^{-3} arising in mid-August yielded a grazing rate Grz of 2.8×10^{-4} d^{-1}. As the ZL concentration was still nearly 50 μmol N m^{-3} in the upper 50 m, the grazed amount of fPON was 0.014 μmol N m^{-3} d^{-1} at the flux peak. The grazed ratio of 0.028 d^{-1} based on the above estimate was an order of magnitude smaller than the decomposition rate (see Section 5.3). This result indicated that the impact of zooplankton grazing on ice-derived PON was negligible, at least in the NAP region. In addition,

806 zooplankton would not efficiently capture fast-sinking aggregates as shown in Lake Saroma
807 (Nishi and Tabeta, 2005). Suspended algae are rather preferable for zooplankton growth
808 (Michel et al., 1996).
809

6. Summary

Biogeochemical structures in the western Arctic were addressed using a sea ice-ocean modeling approach. In the present work, the sea ice ecosystem with ice algal activity was newly incorporated into a pelagic marine ecosystem model. We assumed that ice algae could utilize nutrients (nitrate, ammonium, and silicate) both in the skeletal layer of sea ice and in the ocean surface layer (i.e., seawater nutrients). The ratio of the nutrient source varied depending on ice algal biomass. This "hybrid-type" nutrient uptake formulation is an option to represent more realistic characteristics of ice algal biology.

The modeled ice algal primary production demonstrated noticeable interannual variability as suggested by previous sediment trap analyses in the NAP region. It was found that year-to-year changes in ice algal production were closely related to pan-Arctic wind patterns. In winter 2010–2011, strong easterly winds around the Beaufort High induced basin-ward Ekman transport of shelf-origin surface water and vertical turbulent mixing with underlying nutricline waters. The higher nitrate concentrations were then distributed in the southern Beaufort Sea and the Chukchi Borderland. On the other hand, in winter 2011–2012, northwesterly winds associated with an extension of the Siberian High distributed oligotrophic water from the central Canada Basin toward the northern Chukchi shelf. Hence, ice algal productivity in the NAP region was suppressed by a deeper nutricline, in addition to cloud shading of solar irradiance, until early summer.

The modeled summer biogenic particle flux in the NAP region was comparable with the sediment trap data in 2011 and but was remarkably overestimated in 2012. In summer 2012, lateral advection processes resulted in the enhanced PON flux, because the ice-ocean flux exceeded ice algal production in the same location. In August, westerly winds intensified in the

southern part of the cyclone transported the shelf-origin ice algal patches toward the NAP region. This cyclone event may have caused the model biases on sea ice motion and biogenic particle flux. We further considered several model uncertainties through the sensitivity experiments. The modeled ice algal biomass was highly sensitive to optimum light intensity. PON flux in the water column varied depending on particle sinking speed in addition to ice algal productivity. The impacts of various grazing processes on PON flux were relatively minor within the present cases. However, more possibilities should also be addressed in future studies. Successive observations and model improvements are indispensable to gather ubiquitous findings on ice-related biological processes.

Acknowledgements

This study is supported by the Grant-in-Aid for Scientific Research of Japan Society for the Promotion of Science (JSPS) (KAKENHI 22221003, 26800248, and 15H01736) and the GRENE Arctic Climate Change Research Project. Modeling experiments were executed using the Earth Simulator of Japan Agency for Marine-Science and Technology (JAMSTEC).

References

Aota, M. and Ishikawa, M.: On the extinction coefficient of sea ice, Low Temperature Science Series A., 40, 127–135, 1982.

Arrigo, K., Kremer, J. N., and Sullivan, C. W.: A simulated Antarctic fast ice ecosystem, J. Geophys. Res., 98, 6929–6946, 1993.

Arrigo, K. R., Mock T., and Lizotte, M. P.: Primary producers and sea ice. In: Thomas, D. N., Dieckmann, G. S. (Eds.), Sea Ice. Wiley-Blackwell, Oxford, pp. 283–325, 2010.

Baker, E. T., Milburn, H. B., and Tennant, D. A.: Field assessment of sediment trap efficiency under varying flow conditions, J. Mar. Res., 46, 573–592, 1998.

Bitz, C. M., Holland, M. M., Weaver, A. J., and Eby, M.: Simulating the ice-thickness distribution in a coupled climate model, J. Geophys. Res., 106, 2441–2463, 2001.

Bitz, C. M. and Lipscomb, W. H.: An energy-conserving thermodynamic model of sea ice, J. Geophys. Res., 104, 15,669–15,677, 1999.

Bluhm, B. A., Gradinger, R. R., Schnack-Schiel, S. B.: Sea ice meio- and macro-fauna. In: Thomas, D. N., Dieckmann, G. S. (Eds.), Sea Ice. Wiley-Blackwell, Oxford, pp. 357–393, 2010.

Boetius, A. et al.: Export of algal biomass from the melting Arctic sea ice, Science, 339, 1430–1432, 2013.

Cota, G. F., Legendre, L., Gosselin, M., and Ingram, R. G.: Ecology of bottom ice algae: I. Environmental controls and variability, J. Mar. Sys., 2, 257–277, 1991.

Cota, G. F. and Smith, R. E. H.: Ecology of bottom ice algae: II. Dynamics, distributions and productivity, J. Mar. Sys., 2, 279–295, 1991.

871 Cremer, H: Distribution patterns of diatom surface sediment assemblages in the Laptev Sea
872 (Arctic Ocean). Mar. Micropal., 38, 39–67, 1999.
873 Deal, C., Jin, M., Elliot S., Hunke, E., Maltrud, M., and Jeffery, N.: Large-scale modeling of
874 primary production and ice algal biomass within arctic sea ice in 1992, J. Geophys. Res.,
875 116, C07004, doi:10.1029/2010JC006409, 2011.
876 Dupont, F.: Impact of sea-ice biology on overall primary production in a biophysical model of
877 the pan-Arctic Ocean, J. Geophys. Res., 117, C00D17, doi:10.1029/2011JC006983, 2012.
878 Fahl, K. and Nöthig, E.-M.: Lithogenic and biogenic particle fluxes on the Lomonosov Ridge
879 (central Arctic Ocean) and their relevance for sediment accumulation: Vertical vs. lateral
880 transport, Deep Sea Res- I, 54, 1256–1272, 2007.
881 Forest, A., et al.: Particulate organic carbon fluxes on the slope of the Mackenzie Shelf
882 (Beaufort Sea): Physical and biological forcing of shelf-basin exchanges. J. Mar. Sys., 68,
883 39–54, 2007.
884 Garcia, H. E., Locarnini, R. A., Boyer, T. P., Antonov, J. I., Baranova, O. K., Zweng, M. M.,
885 Reagan, J. R., and Johnson, D. R.: World Ocean Atlas 2013, Volume 4: Dissolved Inorganic
886 Nutrients (phosphate, nitrate, silicate). Levitus, S., Ed., Mishonov, A. Technical Ed.;
887 NOAA Atlas NESDIS, 76, 25pp., 2013.
888 Gardner, D. H.: The effect of tilt on sediment trap efficiency, Deep Sea Res.-A, 32, 349–361,
889 1985.
890 Gosselin, M., Levasseur, M., Wheeler, P. A., Horner, R. A., and Booth, B. C.: New
891 measurements of phytoplankton and ice algal production in the Arctic Ocean, Deep Sea
892 Res.-II, 44, 1623–1644, 1997.

893 Gradinger, R.: Sea-ice algae: Major contributors to primary production and algal biomass in the
894 Chukchi and Beaufort Seas during May/June 2002, Deep Sea Res.-II, 56, 1201–1212, 2009.
895 Haas, C., Hendricks, S., Eicken, H., and Herber, A.: Synoptic airborne thickness surveys reveal
896 state of Arctic sea ice cover, Geophys. Res. Lett., 37, L09501, doi:10.1029/2010GL042652,
897 2010.
898 Hasumi, H.: CCSR Ocean Component Model (COCO) version 4.0, Center for Climate System
899 Research Report, Univ. of Tokyo, 25, 103pp., 2006.
900 Honda, M. C., Kawakami, H., Watanabe, S., and Saino, T.: Concentration and vertical flux of
901 Fukushima-derived radiocesium in sinking particles from two sites in the Northwestern
902 Pacific Ocean, Biogeosciences, 10, 3525–3534, doi:10.5194.bg-10-3525-2013, 2013.
903 Honjo, S., et al.: Biological pump processes in the cryopelagic and hemipelagic Arctic Ocean:
904 Canada Basin and Chukchi Rise, Prog. Oceanogr., 85, 137–170, 2010.
905 Hunke, E. C. and Dukowicz, J. K.: An elastic-viscous-plastic model for sea ice dynamics, J.
906 Phys. Oceanogr., 27, 1849–1867, 1997.
907 Hwang, J., Kim, M., Manganini, S. J., McIntyre, C. P., Haghipour, N., Park, J. J., Krishfield, R.
908 A., Macdonald, R. W., McLaughlin, F. A., and Eglinton, T. I.: Temporal and spatial
909 variability of particle transport in the deep Arctic Canada Basin, J. Geophys. Res., 120,
910 2784–2799, doi:10.1002/2014JC010643, 2015.
911 Ikenoue, T., Bjorklund, K. R., Kruglikova, S. B., Onodera, J., Kimoto, K., and Harada, N.: Flux
912 variations and vertical distributions of siliceous Rhizaria (Radiolaria and Phaeodaria) in the
913 western Arctic Ocean: indices of environmental changes, Biogeosciences, 12, 2019–2046,
914 doi:10.5194/bg-12-2019-2015, 2015.

915 Jin, M., Deal, C. J., Wang, J., Shin, K.-H., Tanaka, N., Whitledge, T. E., Lee, S. H., Gradinger,
916 R. R.: Controls of the landfast ice-ocean ecosystem offshore Barrow, Alaska, Ann. Glaciol.,
917 44, 63–72, 2006.
918 Jin, M., Deal, C., Lee, S. H., Elliott, S., Hunke, E., Maltrud, and M., Jeffery, N.: Investigation
919 of Arctic sea ice and ocean primary production for the period 1992-2007 using a 3-D global
920 ice-ocean ecosystem model, Deep Sea Res.-II, 81–84, 28–35,
921 doi:10.1016/j.dsr2.2011.06.003, 2012.
922 Kishi, M. J., et al.: NEMURO–a lower trophic level model for the North Pacific marine
923 ecosystem, Ecol. Model., 202, 12–25, 2007.
924 Lalande, C., Nöthig, E.-M., Somavilla, R., Bauerfeind, E., Shevchenko, V., and Okolodkov, Y.:
925 Variability in under-ice export fluxes of biogenic matter in the Arctic Ocean, Global
926 Biogeochem. Cycles, 28, doi:10.1002/2013GB004735, 2014.
927 Lavoie, D., Denman, K., and Michel, C.: Modeling ice algal growth and decline in a seasonally
928 ice-covered region of the Arctic (Resolute Passage, Canadian Archipelago), J. Geophys.
929 Res., 110, C11009, doi:10.1029/2005JC002922, 2005.
930 Lavoie, D., Denman, K. L., and Macdonald, R. W.: Effects of future climate change on primary
931 productivity and export fluxes in the Beaufort Sea, J. Geophys. Res., 115, C04018,
932 doi:10.1029/2009JC005493, 2010.
933 Leonard, B. P., MacVean, M. K., and Lock, A. P.: The flux-integral method for multi-
934 dimensional convection and diffusion, NASA Tech. Memo, 106679/ICOMP-94-13, NASA,
935 Washington, D. C., 1994.
936 Leventer, A.: Particulate flux from sea ice in polar waters. In: Thomas, D. N. and Dieckmann G.
937 S. (Eds.), Sea Ice. Wiley-Blackwell, Oxford, pp. 303–332, 2003.

938 Llinas, L., Pickart, R. S., Mathis, J. T., and Smith, S. L.: Deep Sea Res.-II, 56, 1290–1304, 2009.
939 Lipscomb, W. H.: Remapping the thickness distribution in sea ice models, J. Geophys. Res.,
940 106, 13,989–14,000, 2001.
941 Matsuno, K., Yamaguchi, A., Fujiwara, A., Onodera, J., Watanabe, E., Harada, N., and Kikuchi,
942 T.: Seasonal changes in the population structure of dominant planktonic copepods collected
943 using a sediment trap moored in the western Arctic Ocean, J. Natural History, in press.,
944 2015.
945 McLaughlin, F. A. and Carmack, E. C.: Deepening of the nutricline and chlorophyll maximum
946 in the Canada Basin interior, 2003–2009, Geophys. Res. Lett., 37, L24602,
947 doi:10.1029/2010GL045459, 2010.
948 Michel, C., Legendre, L. L., Therriault, J.-C., Demers, S., and Vandevelde T.: Springtime
949 coupling between ice algal and phytoplankton assemblages in southeastern Hudson Bay,
950 Canadian Arctic, Polar Biol., 13, 441–449, 1993.
951 Michel, C., Legendre, L., Ingram, R. G., Gosselin, M., and Levasseur, M.: Carbon budget of
952 sea-ice algae in spring: Evidence of a significant transfer to zooplankton grazers, J.
953 Geophys. Res., 101, 18,345–18,360, 1996.
954 Nishi, Y., and Tabeta, S.: Analysis of the contribution of ice algae to the ice-covered ecosystem
955 in Lake Saroma by means of a coupled ice-ocean ecosystem model. J. Mar. Sys., 55, 249–
956 270, 2005
957 Nishino, S., Kikuchi, T., Yamamoto-Kawai, M., Kawaguchi, Y., Hirawake, T., and Itoh, M.:
958 Enhancement/reduction of biological pump depends on ocean circulation in the sea-ice
959 reduction regions of the Arctic Ocean. J. Oceanogr., 67, 305–314, 2011.

960 Noh, Y. and Kim, H. J.: Simulations of temperature and turbulence structure of the oceanic
961 boundary layer with the improved near-surface process, J. Geophys. Res., 104, 15,621–
962 15,634, 1999.
963 Onodera, J., Watanabe, E., Harada, N., and Honda, M. C.: Diatom flux reflects water-mass
964 conditions on the southern Northwind Abyssal Plain, Arctic Ocean, Biogeosciences, 12,
965 1373–1385, doi:10.5194/bg-12-1373-2015, 2015.
966 Peralta-Ferriz, C. and Woodgate, R. A.: Seasonal and interannual variability of pan-Arctic
967 surface mixed layer properties from 1979 to 2012 from hydrographic data, and the
968 dominance of stratification for multiyear mixed layer depth shoaling, Prog. Oceanogr., in
969 press, doi:10.1016/j.pocean.2014.12.005, 2015.
970 Pogson, L., Tremblay, B., Lavoie, D., Michel, C., and Vancoppenolle, M.: Development and
971 validation of a one-dimensional snow-ice algae model against observations in Resolute
972 Passage, Canadian Arctic Archipelago, J. Geophys. Res., 116, C040110,
973 doi:10.1029/2010JC006119, 2011.
974 Proshutinsky, A. Y. and Johnson, M. A.: Two circulation regimes of the wind-driven Arctic
975 Ocean, J. Geophys. Res., 102, 12,493–12,514, 1997.
976 Proshutinsky, A., Krishfield, R., Timmermans, M.-L., Toole, J., Carmack, E., McLaughlin, F.,
977 Williams, W. J., Zimmermann, S., Itoh, M., and Shimada, K.: Beaufort Gyre freshwater
978 reservoir: State and variability from observations, J. Geophys. Res., 114, C00A10,
979 doi:10.1029/2008JC005104, 2009.
980 Saha, S., et al.: The NCEP Climate Forecast System reanalysis. Bull. Am. Meteorol. Soc., 91,
981 1015–1057, doi:10.1175/2010BAMS3001.1, 2010.

982 Simmonds, I. and Rudeva, I.: The great Arctic cyclone of August 2012, Geophys. Res. Lett., 39,
983 L23709, doi:10.1029/2012GL054259, 2012.
984 Spall, M. A., Pickart, R. S., Frantantoni, P. S., and Plueddemann, A. J.: Western Arctic
985 shelfbreak eddies: Formation and transport, J. Phys. Oceanogr., 38, 1644–1668, 2008.
986 Steele, M., Morley, R., and Ermold, W.: PHC: A global ocean hydrography with a high-quality
987 Arctic Ocean, J. Clim., 14, 2079–2087, 2001.
988 Tedesco, L., Vichi, M., Haapala, J., and Stipa, T.: A dynamic Biologically Active Layer for
989 numerical studies of the sea ice ecosystem, Ocean Model., 35, 89–104, 2010.
990 Vancoppenolle, M., Goosse, H., de Montety A., Fichefet, T., Tremblay, B., and Tison, J. –L.:
991 Modeling brine and nutrient dynamics in Antarctic sea ice: The case of dissolved silica, J.
992 Geophys. Res., 115, C02005, doi:10.1029/2009JC005359.
993 Wassmann, P.: Arctic marine ecosystems in an era of rapid climate change. Prog. Oceanogr.. 90,
994 1–17, 2011.
995 Watanabe, E.: Beaufort shelf break eddies and shelf-basin exchange of Pacific summer water in
996 the western Arctic Ocean detected by satellite and modeling analyses, J. Geophys. Res.,
997 116, C08034, doi:10.1029/2010JC006259, 2011.
998 Watanabe, E., Kishi, M. J., Ishida, A., and Aita, M. N.: Western Arctic primary productivity
999 regulated by shelf-break warm eddies, J. Oceanogr., 68, 703–718, doi:10.1007/s10872-012-
1000 0128-6, 2012.
1001 Watanabe, E., Onodera, J., Harada, N., Honda, M. C., Kimoto, K., Kikuchi, T., Nishino, S.,
1002 Matsuno, K., Yamaguchi, A., Ishida, A., and Kishi, M. J.: Enhanced role of eddies in the
1003 Arctic marine biological pump, Nature Comm., 5, doi:10.1038/ncomms4950, 2014.

1004 Woodgate, R. A., Aagaard, K., and Weingartner, T. J.: Monthly temperature, salinity, and
1005 transport variability of the Bering Strait through flow, Geophys. Res. Lett., 32, L04601,
1006 doi:10.1029/2004GL021880, 2005.
1007 Yamazaki, A., Inoue, J., Dethloff, K., Maturilli, M., and König-Langlo, G.: Impact of
1008 radiosonde observations on forecasting summertime Arctic cyclone formation, J. Geophys.
1009 Res., 120, doi:10.1002/2014JD022925, 2015.
1010 Yang, J.: Seasonal and interannual variability of downwelling in the Beaufort Sea, J. Geophys.
1011 Res., 114, C00A14, doi:10.1029/2008JC005084, 2009.
1012 Zhang, J., Spitz, Y. H., Steele, M., Ashjian, C., Campbell, R., Berline, L., and Matrai, P.:
1013 Modeling the impact of declining sea ice on the Arctic marine planktonic ecosystem, J.
1014 Geophys. Res., 115, C10015, doi:10.1029/2009JC005387, 2010.
1015 Zhang, J., Lindsay, R., Schweiger, A., and Steele, M.: The impact of an intense summer cyclone
1016 on 2012 Arctic sea ice retreat, Geophys. Res. Lett., 40, doi:10.1002/grl.50190, 2013.
1017 Zhang, J., Ashjian, C., Campbell, R., Hill, V., Spitz, Y. H., and Steele, M.: The great 2012 Arctic
1018 Ocean summer cyclone enhanced biological productivity on the shelves, J. Geophys. Res.,
1019 119, 297–312, 2014.
1020

1021 **Table captions**

1022 **Table 1.** Parameters in the sea ice ecosystem model. The values of ice algae are same as those
1023 of large phytoplankton in the original NEMURO model (Kishi et al., 2007). The PAR fraction
1024 followed Zhang et al. (2010), and the light extinction rates were derived from Aota and
1025 Ishikawa (1982). The parameter values of nitrogen and silicon flows in the skeletal layer were
1026 same as those in the water column, which were also provided by Kishi et al. (2007).

1027

1028 **Table 2.** Monthly mean values of NCEP/CFSR cloud fraction (n. d.), downward shortwave
1029 radiation (W m^{-2}), 10 m wind speed (m s^{-1}), snow depth (cm), sea ice thickness (cm), and sea
1030 ice concentration (n. d.) averaged in the NAP region. 2011 (2012) corresponds to the period
1031 from October 2010 (2011) to September 2011 (2012) to compare the model results.

1032

1033 **Figure captions**

1034 **Figure 1.** Bathymetry of the pan-Arctic sea ice-ocean model COCO. Location of Station NAP
1035 is indicated by a red dot in the left enlarged view. The NAP region defined in the present study
1036 is enclosed by 74°–76°N and 159°–165°W. The model integration period covers 33 years from
1037 1979 to 2011 only for the physical oceanographic part using the 25 km resolution version, and
1038 the obtained fields are given as initial condition for one year experiment from October 2010
1039 (2011) to September 2011 (2012) in the 2011 (2012) case using the 5 km resolution version
1040 with marine ecosystem components.

1041

1042 **Figure 2.** Schematic image and configuration of the Arctic NEMURO model. Nitrogen and
1043 silicon flows are composed of photosynthesis (Photo), shell formation (Shell), respiration (Res),
1044 excretion (Exc), mortality (Mor), grazing (Grz), predation (Prd), egestion (Ege), decomposition
1045 (Dec), remineralization (Rem), nitrification (Nit), and sinking (Sink). Ice algal habitat is
1046 confined to the skeletal layer of sea ice bottom. Ice-related fauna (IF) is calculated only in a
1047 sensitivity experiment (Case 4). Exchange of biogeochemical variables with the pelagic
1048 ecosystem is allowed at the ice-ocean interface.

1049

1050 **Figure 3.** Relationships of (a) light extinction rate (non-dimensional (n. d.)) v. s. thickness of
1051 (dashed line) snow and (solid line) sea ice (cm), (b) light condition term (n. d.) v. s. light
1052 intensity (PAR) (W m^{-2}), (c) ice nutrient uptake ratio RN_{upSKL} (n. d.) v. s. ice algal biomass
1053 (mmol N m^{-2}), (d) nitrate condition term (n. d.) v. s. nitrate concentration (mmol N m^{-3}), and (e)
1054 sinking speed of PON derived from (solid line) ice algae and (dashed line) pelagic plankton

1055 groups (m d^{-1}) v. s. depth in the water column (m), respectively, in the Arctic NEMURO model.
1056 See more information in Section 2.2.
1057
1058 **Figure 4.** Seasonal transition of daily mean modeled variables in the NAP region. (a) Sea ice
1059 concentration (n. d.), (b) sea ice thickness (cm), (c) thermal growth rate of sea ice (cm d^{-1}), (d)
1060 divergence of sea ice velocity (d^{-1}), (e) Ekman upwelling velocity diagnosed using ocean
1061 surface stress fields (m d^{-1}), and (f) vertical diffusivity at the depth of 20 m (cm^2 s^{-1}) in the
1062 2011 (red line) and 2012 (blue line) cases. Note that negative values in (c), (d), and (e)
1063 correspond to sea ice melting, convergence of sea ice velocity, and Ekman downwelling,
1064 respectively. Vertical diffusivity in (f) is shown in a logarithm scale.
1065
1066 **Figure 5.** Modeled annual primary production of ice algae in the (a) 2011 and (b) 2012 cases
1067 (mmol N m^{-2}). The difference between the two cases is shown in (c). Yellow dots denote the
1068 location of Station NAP. White dots represent the eastern and western limits of 75°N section in
1069 Figs. 6b-c.
1070
1071 **Figure 6.** Modeled seasonal transition of ice algal biomass (a) in the NAP region and (b-c)
1072 along the 75°N line (mmol N m^{-2}). Sea floor depths along the east-west section are also plotted
1073 (m). Red line in (a) and Hovmöller diagram in (b) correspond to the 2011 case. Blue line in (a)
1074 and the diagram in (c) correspond to the 2012 case. The content of 1 mmol N m^{-2} in the sea ice
1075 column corresponds to the concentration of 50 mmol N m^{-3} when the skeletal layer thickness is
1076 set to 2 cm.
1077

1078 **Figure 7.** Modeled seasonal transition of (a) light intensity (PAR) in the skeletal layer (W m^{-2}),
1079 (b) light condition term (n. d.), (c) ice nutrient uptake ratio RN_{upSKL} (n. d.), and (d) nitrate
1080 condition term (n. d.) in the NAP region in the 2011 (red line) and 2012 (blue line) cases. Each
1081 term in (b-d) corresponds to ice algal value. In (d), the condition terms in the (thick lines)
1082 skeletal layer and (thin lines) ocean surface layer are shown.
1083
1084 **Figure 8.** Modeled seasonal transition of nitrate concentration (a) in the skeletal layer (mmol N
1085 m^{-2}) and (b-c) in the top 100 m of water columns (mmol N m^{-3}). Red line in (a) and vertical
1086 profile in (b) correspond to the 2011 case. Blue line in (a) and the profile in (c) correspond to
1087 the 2012 case.
1088
1089 **Figure 9.** Modeled (a-b) primary production rate of ice algae and (c-d) PON flux in the NAP
1090 region in the (a, c) 2011 and (b, d) 2012 cases (μmol N m^{-2} d^{-1}). In (a-b), the daily rate of total
1091 primary production (black lines) and those derived from nutrients in the skeletal layer (light
1092 blue lines) and water column (purple lines) are shown. The export flux of PON from the sea ice
1093 bottom to the underlying water column is overlaid by olive lines. In (c-d), the total simulated
1094 (black lines) and observed (gray bars) PON fluxes at 180 m are compared. The fluxes
1095 originating from ice algae (green lines) and pelagic plankton groups (orange lines) are also
1096 shown.
1097

Figure 10. (a-b) (contours) Sea level pressure (SLP) (hPa) and (vectors) wind stress averaged (a) from November 2010 to January 2011 and (b) from November 2011 to January 2012. SLP is obtained from the NCEP/CFSR dataset, and wind stress vectors are calculated from the SLP field using the AOMIP formulation. Unit vector of wind stress is 0.1 Pa. Direction of (c-d) satellite-based and (e-f) modeled sea ice velocity in the NAP region (degree). Only daily averages whose velocity exceeded 5 cm s^{-1} in the (c, e) 2011 and (d, f) 2012 periods are plotted. Positive (negative) values of the direction correspond to northward (southward), and solid (dashed) bars indicate westward (eastward) motions, respectively. For example, a solid bar of −45° means southwestward direction of 225 °T.

Figure 11. Modeled nitrate concentration (mmol N m^{-3}). The daily mean fields averaged in the top 30 m of water columns on March 1 in the (a) 2011 and (b) 2012 cases are shown in the upper panels. In these experiments, a passive tracer is provided from the ocean surface to sea floor of 100–200 m depth along shelf-basin boundary sandwiched by white contours. Black contours correspond to a tracer value of 0.2 (0–30 m average). Orange lines denote the isobaths of 1,000 and 3,000 m. The vertical profile in the NAP region on (black) October 1, (blue) December 1, and (magenta) February 1 in the (c) 2011 and (d) 2012 cases are shown in the lower panels.

Figure 12. (a) NCEP/CFSR (contours) sea level pressure (hPa) and (shade) sea ice concentration (n. d.) on August 6, 2012. (b) Modeled (contours) PON flux at the depth of 180 m and (vectors) sea ice motion averaged for August 3–10 in the 2012 case. The flux contours of 5, 10, and 20 μmol N m^2 d^{-1} are shown around the Chukchi Borderland. The sea ice motion is

overlaid every ten grid (i.e., approximately 50 km), and its unit vector is 20 cm s^{-1}. Red dots denote the location of Station NAP. August time series of the modeled (c) ice algal biomass (mmol N m^{-2}) and (d) PON flux (μmol N m^{-2} d^{-1}) in the 2012 case (black lines) and the no ice algal activity case (blue lines).

Figure 13. Schematic image of sensitivity experiments. In Case 4, the grazing pressure of ice-related fauna (IF) on ice algae (IA) and the transition from IF to mesozooplankton (ZL) after sea ice melting were calculated for the seeding. In Case 5, a part of IA was treated as large phytoplankton (PL) after sea ice melting. In Case 6, the ZL grazing on fast-sinking Particulate Organic Nitrogen (fPON) was calculated in the water column, and the formulation of slow-sinking one (sPON) was not changed.

Figure 14. Modeled seasonal transition of (a, c, e, g, i, k) ice algal biomass (mmol N m^{-2}) and (b, d, f, h, j, l) PON flux (μmol N m^{-2} d^{-1}) in the NAP region in (a-b) Case 1, (c-d) Case 2, (e-f) Case 3, (g-h) Case 4, (i-j) Case 5, and (k-l) Case 6. Black thin lines correspond to the original 2011 case. The results with I_{opti} of 5 (20) W m^{-2} in Case 1, KN_{upSKL} of 0.5 (1.5) mmol N m^{-2} in Case 2, PON sinking speed of 200 (20) m d^{-1} in Case 3 are shown by magenta (blue) lines, respectively. The biomass of ice-related fauna is shown by an olive line in Case 4.

Table 1

Parameter	Definition	Value	Unit
[Ice algae]			
V_{max}	Maximum phytosynthetic rate at 0 ^oC	0.8	d^{-1}
K_{NO3}	Half saturation constant for nitrate	3.0	mmol-N m^{-3}
K_{NH4}	Half saturation constant for ammonium	0.1	mmol-N m^{-3}
K_{SIL}	Half saturation constant for silicate	6.0	mmol-N m^{-3}
Ψ_{NH4}	Ammonium inhibition coefficient	1.5	$(mmol\text{-}N\ m^{-3})^{-1}$
K_{Gpp}	Temperature coefficient for photosynthetic rate	0.0693	$^oC^{-1}$
I_{opt}	Optimum light intensity	10	W m^{-2}
Res_0	Respiration rate at 0 ^oC	0.03	d^{-1}
K_{Res}	Temperature coefficient for respiration rate	0.0519	$^oC^{-1}$
γ	Extracellular excretion ratio to photosynthesis	0.135	n. d.
Mor_0	Mortality rate at 0 ^oC	0.029	$(mmol\text{-}N\ m^{-3})^{-1}\ d^{-1}$
K_{Mor}	Temperature coefficient for mortality rate	0.0693	$^oC^{-1}$
R_{SiN}	Si:N ratio	2.0	n. d.
[Light property]			
PAR_{frac}	Fraction of PAR to shortwave radiation	0.43	n. d.
k_{snow}	light extinction rate for snow	0.12	cm^{-1}
k_{ice}	light extinction rate for sea ice	0.045	cm^{-1}
[Nitrogen/Silicon flow]			
Nit_0	Nitrification rate at 0 ^oC	0.03	d^{-1}
K_{Nit}	Temperature coefficient for nitrification	0.0693	$^oC^{-1}$
$VP2N_0$	Decomposition rate from PON to ammonium at 0 ^oC	0.1	d^{-1}
$VP2D_0$	Decomposition rate from PON to DON at 0 ^oC	0.1	d^{-1}
$VD2N_0$	Decomposition rate from DON to ammonium at 0 ^oC	0.02	d^{-1}
$VP2Si_0$	Decomposition rate from opal to silicate at 0 ^oC	0.1	d^{-1}
$K_{P2N}/K_{P2D}/K_{D2N}/K_{P2Si}$	Temperature coefficient for decomposition rate	0.0693	$^oC^{-1}$

Table 2

		Oct	Nov	Dec	Jan	Feb	Mar	Apr	May	Jun	Jul	Aug	Sep
Cloud	**2011**	0.98	0.87	0.79	0.79	0.91	0.88	0.72	0.90	0.76	0.92	0.98	0.96
Fraction	**2012**	0.94	0.90	0.67	0.81	0.79	0.56	0.61	0.83	0.88	0.97	0.97	0.96
Shortwave	**2011**	9	0	0	0	4	51	165	236	305	217	102	45
Radiation	**2012**	10	0	0	0	4	62	170	245	264	184	92	46
Wind	**2011**	6.7	5.1	5.0	5.1	6.0	4.3	4.6	4.4	4.5	4.4	5.3	5.4
Speed	**2012**	8.1	5.0	4.8	5.1	4.7	4.5	4.1	3.9	4.7	4.7	7.1	7.1
Snow	**2011**	11	23	32	37	41	44	46	33	0	0	0	0
Depth	**2012**	8	23	22	21	23	23	22	13	0	0	0	0
Sea Ice	**2011**	60	209	216	261	276	281	268	249	228	169	78	0
Thickness	**2012**	60	210	232	271	279	278	286	259	207	141	62	0
Sea Ice	**2011**	0.21	0.89	0.98	0.99	0.99	0.99	0.99	0.99	0.99	0.83	0.19	0
Concentration	**2012**	0.19	0.90	0.98	0.98	0.98	0.98	0.99	0.97	0.87	0.70	0.18	0

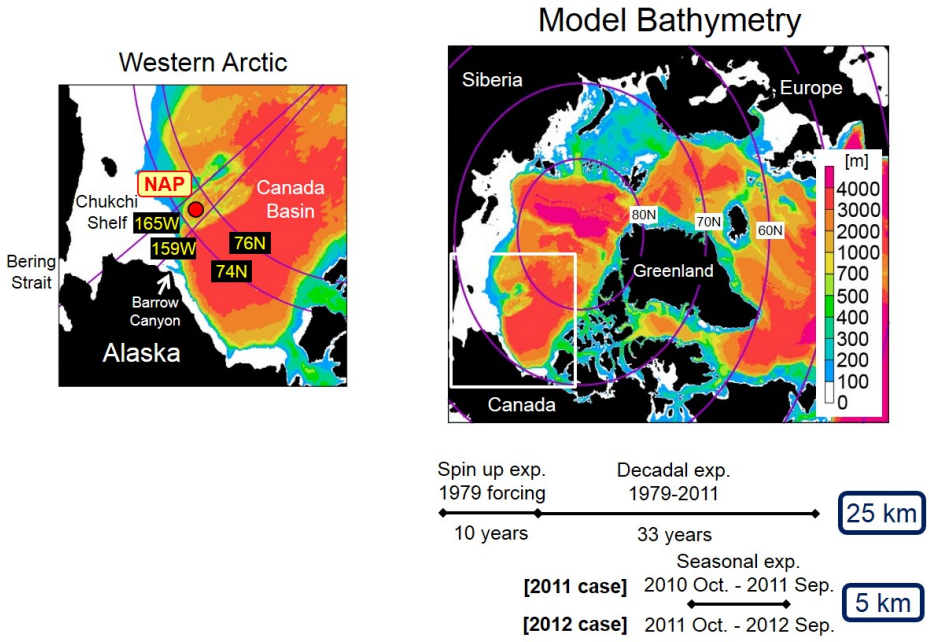
Western Arctic
NAP
Chukchi
Shelf
165W
159W
76N
74N
Canada
Basin
Bering
Strait
Barrow
Canyon
Alaska
Model Bathymetry
Siberia
Europe
80N
70N
60N
Greenland
Canada
[m]
4000
3000
2000
1000
700
500
400
300
200
100
0
Spin up exp.
1979 forcing
10 years
Decadal exp.
1979-2011
33 years
25 km
Seasonal exp.
[2011 case] 2010 Oct. - 2011 Sep.
[2012 case] 2011 Oct. - 2012 Sep.
5 km

Fig. 1.

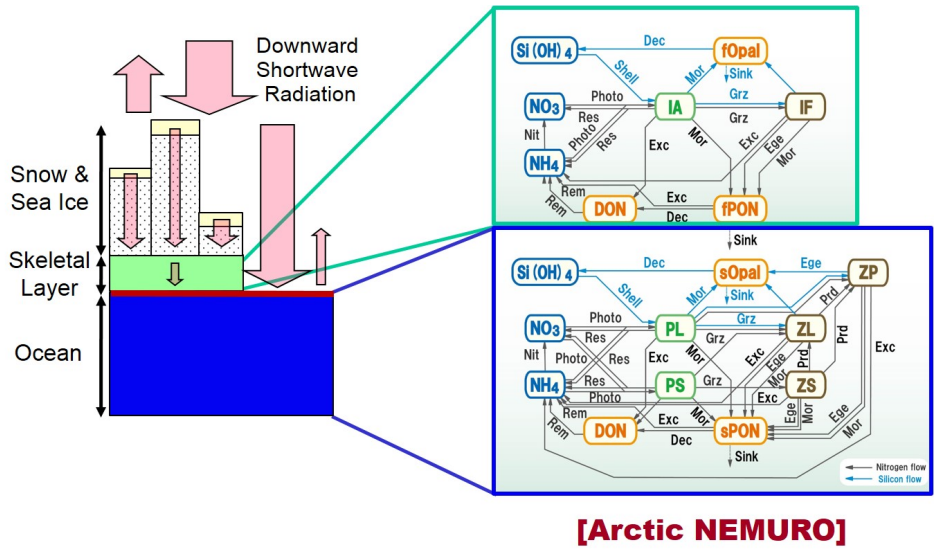
Downward
Shortwave
Radiation
Snow &
Sea Ice
Skeletal
Layer
Ocean
Si(OH)4
NO3
NH4
DON
fPON
fOpal
IA
IF
sPON
sOpal
PL
PS
ZP
ZL
ZS
Dec
Shell
Mor
Sink
Photo
Res
Nit
Exc
Grz
Ege
Prd
Rem
Nitrogen flow
Silicon flow
[Arctic NEMURO]

Fig. 2.

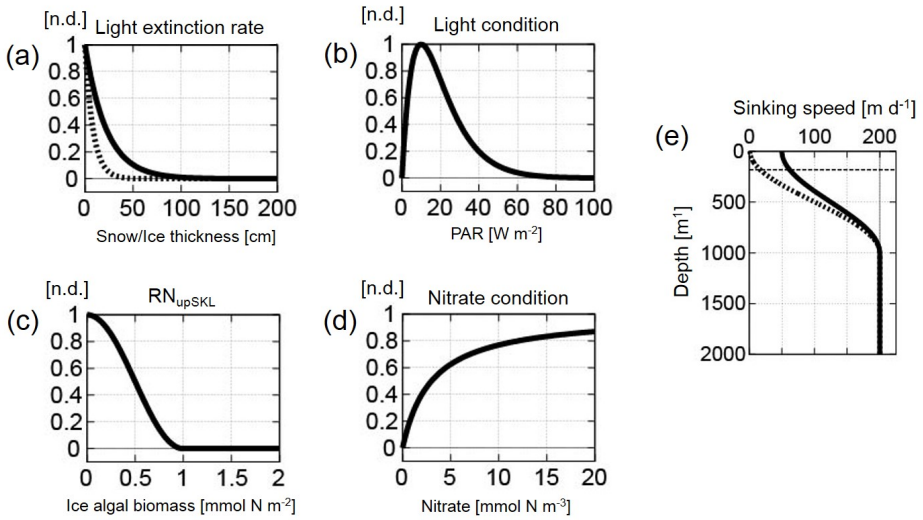
(a)
[n.d.]
Light extinction rate
Snow/Ice thickness [cm]
(b)
[n.d.]
Light condition
PAR [W m-2]
(c)
[n.d.]
RNupSKL
Ice algal biomass [mmol N m-2]
(d)
[n.d.]
Nitrate condition
Nitrate [mmol N m-3]
(e)
Sinking speed [m d-1]
Depth [m-1]

Fig. 3.

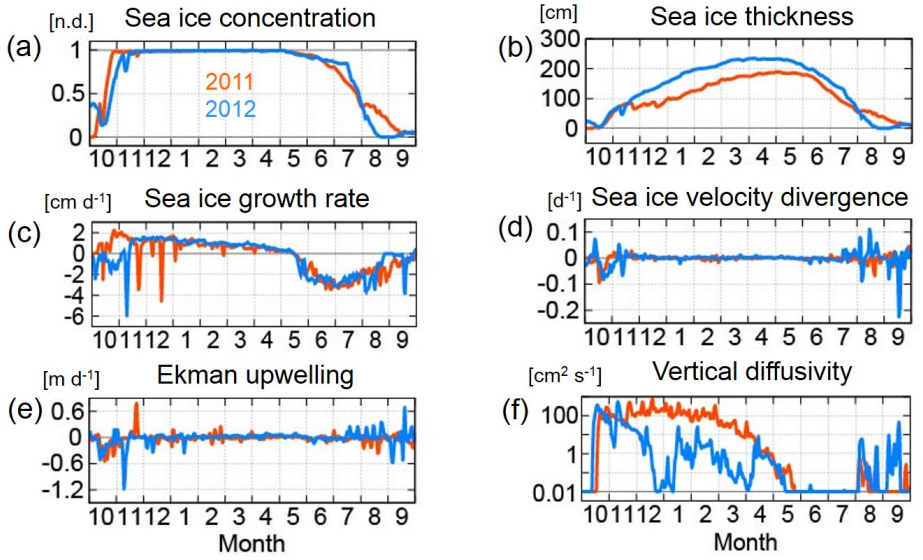
(a)
[n.d.]
Sea ice concentration
2011
2012
(b)
[cm]
Sea ice thickness
(c)
[cm d-1]
Sea ice growth rate
(d)
[d-1]
Sea ice velocity divergence
(e)
[m d-1]
Ekman upwelling
(f)
[cm2 s-1]
Vertical diffusivity
Month
Month

Fig. 4.

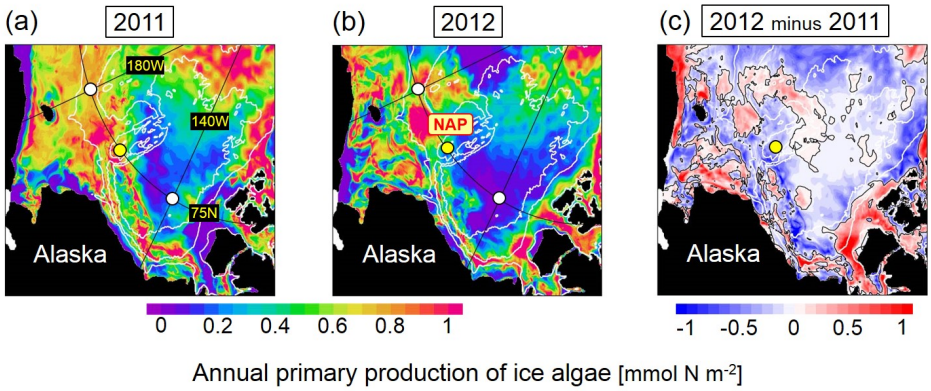
(a)
2011
(b)
2012
(c)
2012 minus 2011
180W
140W
75N
NAP
Alaska
Alaska
Alaska
0
0.2
0.4
0.6
0.8
1
-1
-0.5
0
0.5
1
Annual primary production of ice algae [mmol N m-2]

Fig. 5.

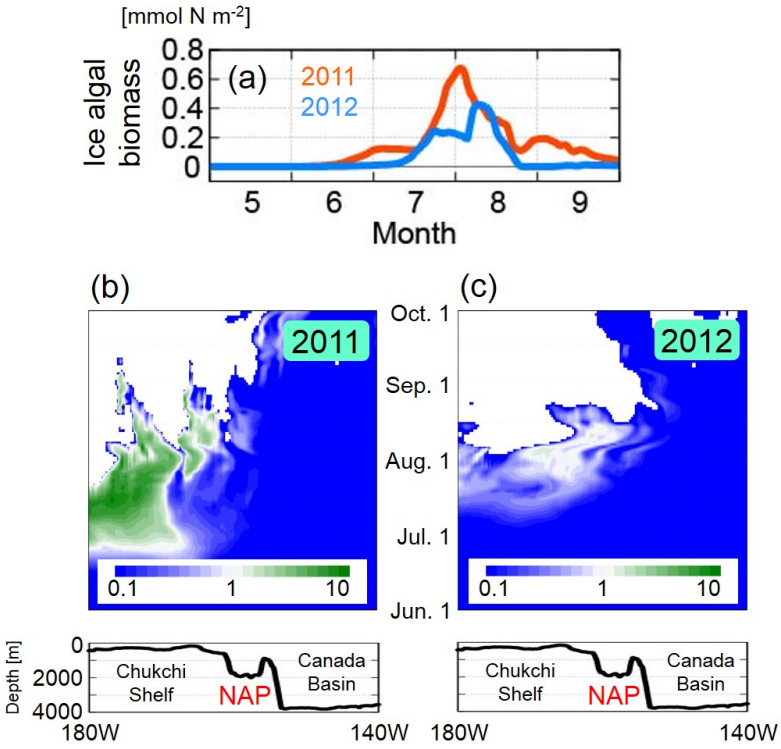
[mmol N m-2]
Ice algal biomass
0.8
0.6
0.4
0.2
0
(a)
2011
2012
5
6
7
8
9
Month
(b)
(c)
2011
2012
Oct. 1
Sep. 1
Aug. 1
Jul. 1
Jun. 1
0.1
1
10
0.1
1
10
Depth [m]
0
2000
4000
Chukchi Shelf
NAP
Canada Basin
180W
140W
Chukchi Shelf
NAP
Canada Basin
180W
140W

Fig. 6.

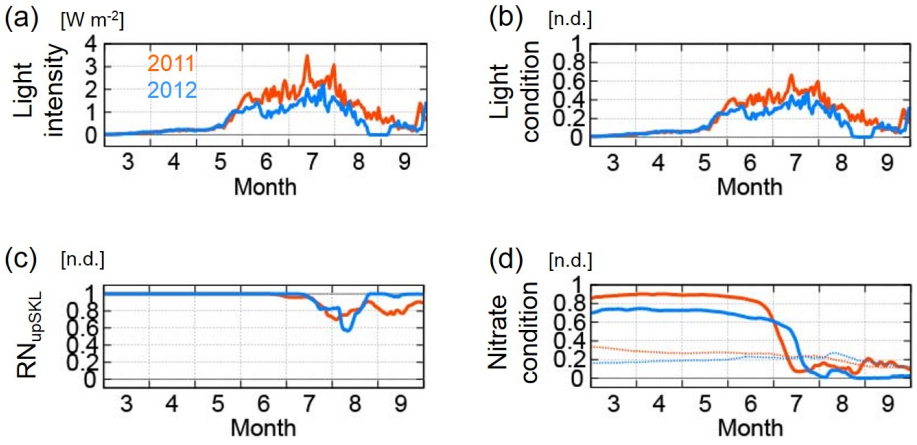
(a) [W m-2]
Light intensity
2011
2012
Month
(b) [n.d.]
Light condition
Month
(c) [n.d.]
RNupSKL
Month
(d) [n.d.]
Nitrate condition
Month

Fig. 7.

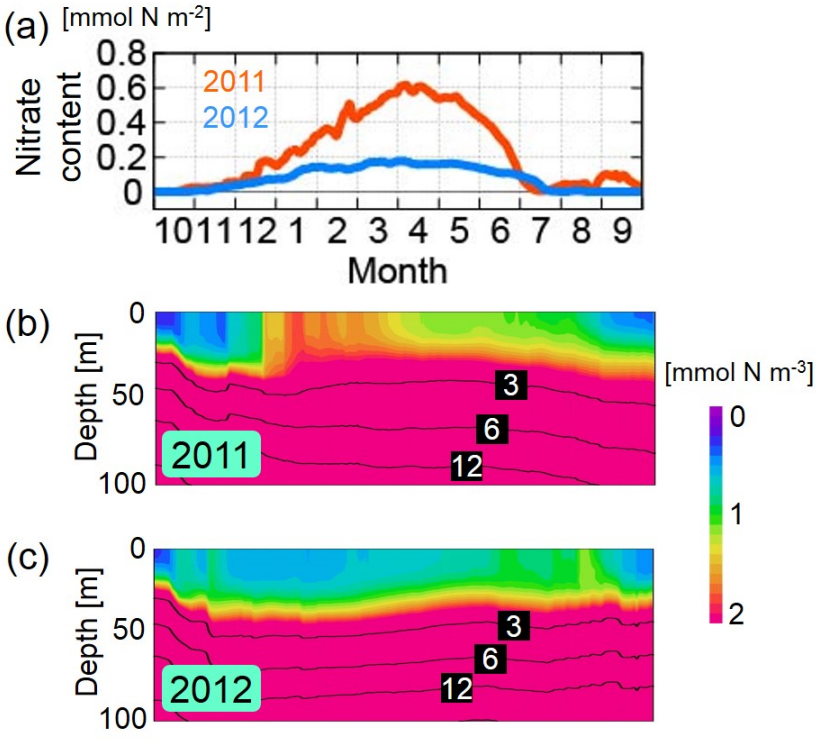
(a) [mmol N m-2]
Nitrate content
2011
2012
Month
(b)
Depth [m]
2011
3
6
12
[mmol N m-3]
(c)
Depth [m]
2012
3
6
12

Fig. 8.

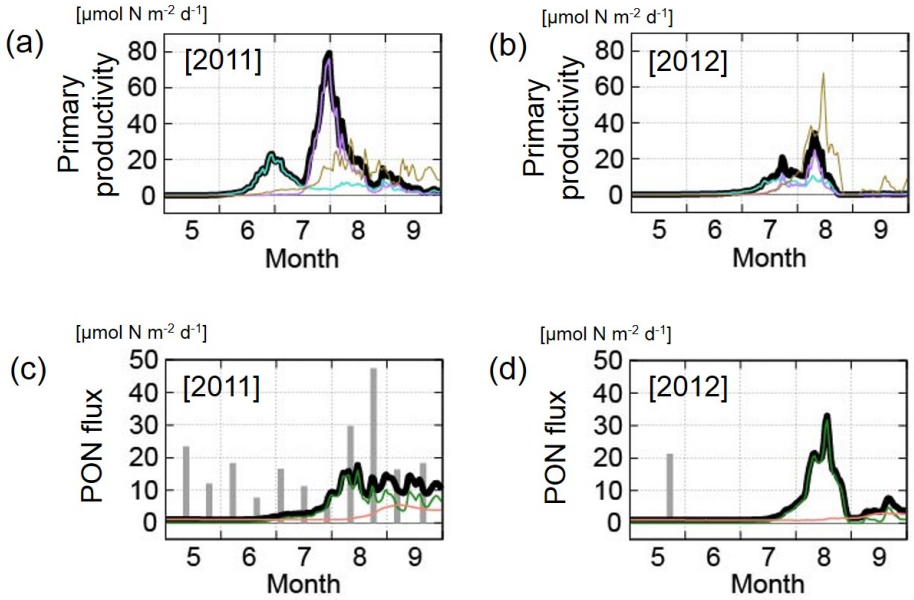
(a)
[μmol N m-2 d-1]
Primary productivity
[2011]
Month
(b)
[μmol N m-2 d-1]
Primary productivity
[2012]
Month
(c)
[μmol N m-2 d-1]
PON flux
[2011]
Month
(d)
[μmol N m-2 d-1]
PON flux
[2012]
Month

Fig. 9.

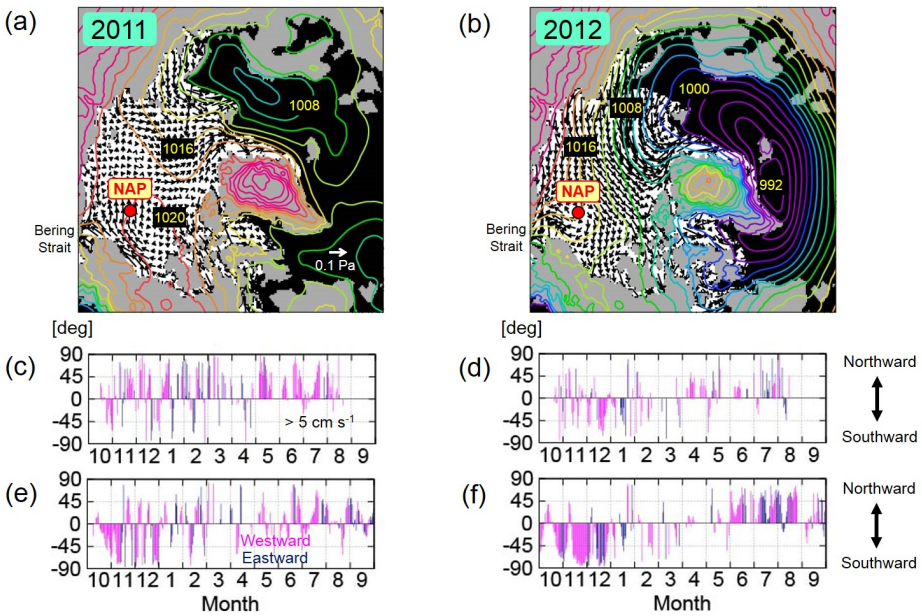
(a)
2011
1008
1016
NAP
1020
Bering Strait
0.1 Pa
(b)
2012
1000
1008
1016
NAP
992
Bering Strait
[deg]
(c)
> 5 cm s-1
(d)
Northward
Southward
(e)
Westward
Eastward
Month
(f)
Northward
Southward
Month

Fig. 10.

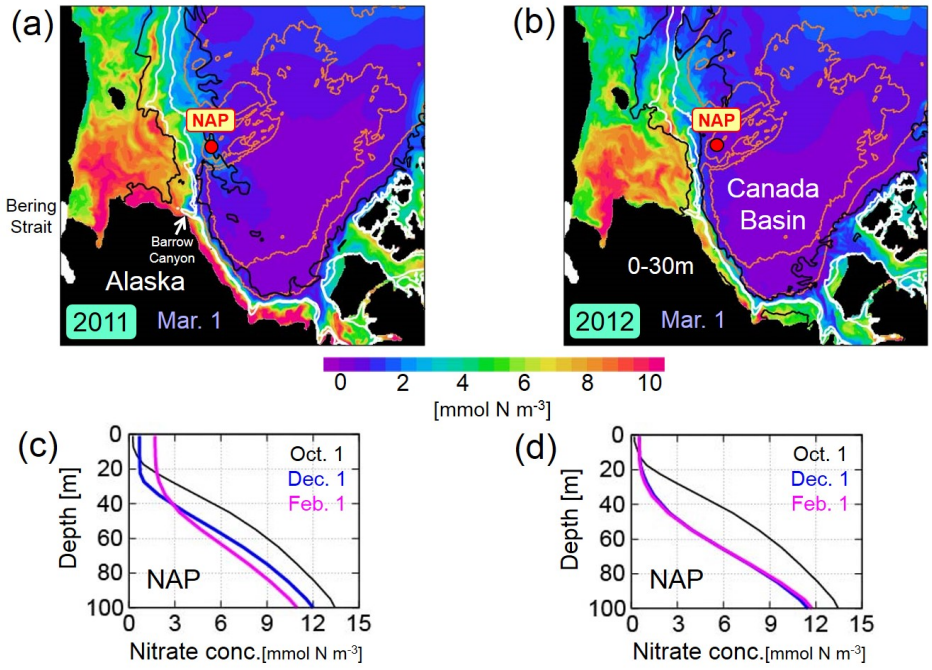
(a)
(b)
NAP
Bering
Strait
Barrow
Canyon
Alaska
2011
Mar. 1
Canada
Basin
0-30m
2012
Mar. 1
0
2
4
6
8
10
[mmol N m-3]
(c)
(d)
Depth [m]
Oct. 1
Dec. 1
Feb. 1
NAP
Nitrate conc.[mmol N m-3]

Fig. 11.

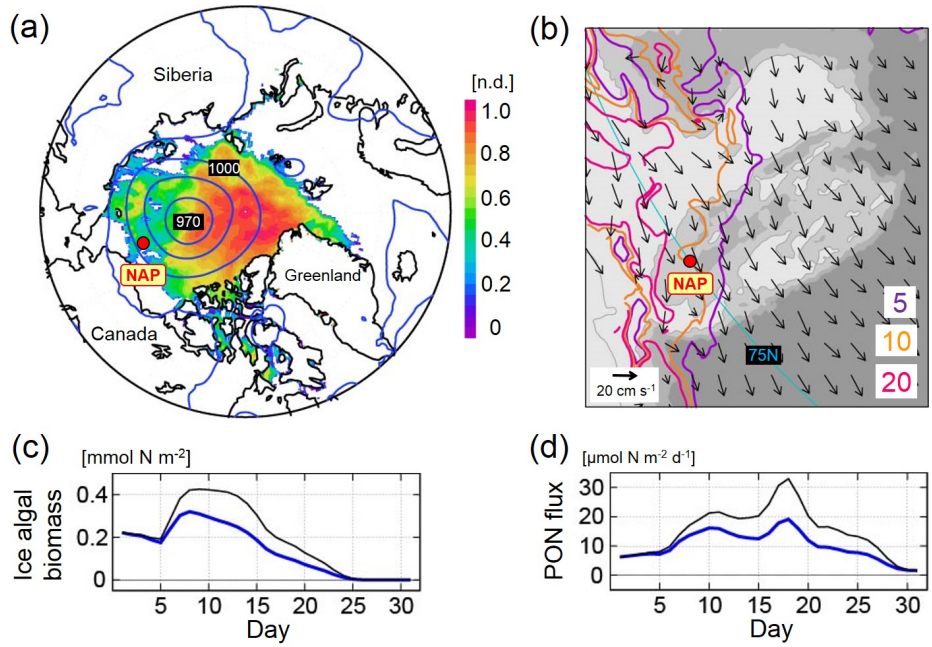
(a)
(b)
Siberia
1000
970
NAP
Greenland
Canada
[n.d.]
1.0
0.8
0.6
0.4
0.2
0
5
10
20
75N
20 cm s-1
(c)
[mmol N m-2]
Ice algal biomass
Day
(d)
[μmol N m-2 d-1]
PON flux
Day

Fig. 12.

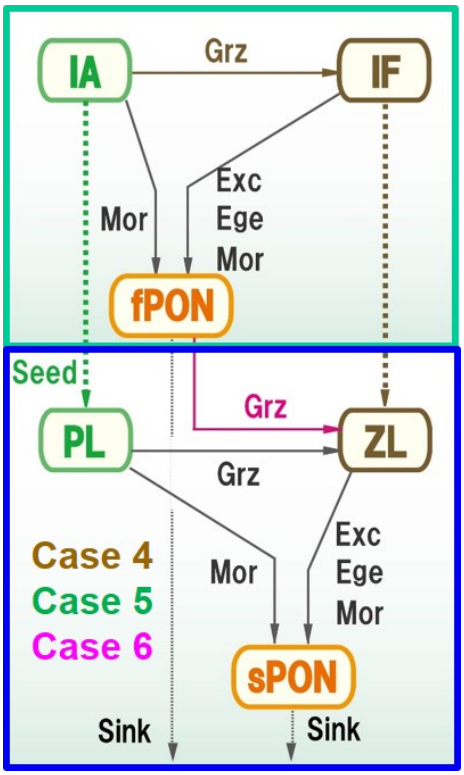
IA
Grz
IF
Exc
Ege
Mor
Mor
fPON
Seed
Grz
PL
ZL
Grz
Case 4
Case 5
Case 6
Mor
Exc
Ege
Mor
sPON
Sink
Sink

Fig. 13.

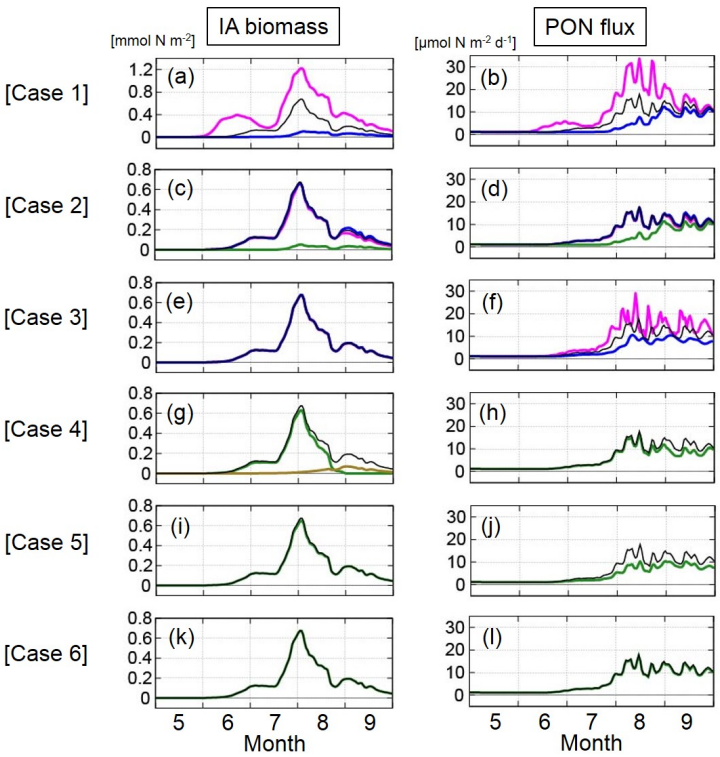
IA biomass
PON flux
[mmol N m-2]
[μmol N m-2 d-1]
[Case 1]
[Case 2]
[Case 3]
[Case 4]
[Case 5]
[Case 6]
(a)
(b)
(c)
(d)
(e)
(f)
(g)
(h)
(i)
(j)
(k)
(l)
Month
Month

Fig. 14.